A new very high-order finite-difference method for linear stability analysis and bi-orthogonal decomposition of hypersonic boundary layer flow

Zihao Zou *, Xiaolin Zhong

Mechanical and Aerospace Engineering Department, University of California Los Angeles, Los Angeles, CA 90095, USA

A R T I C L E   I N F O

A B S T R A C T

Precisely predicting laminar-turbulence transition locations is essential for improvements in hypersonic vehicle design related to flow control and heat protection. Currently state-of-the-art e^N prediction method requires the evaluation of discrete normal modes F and S for the growth rate of instability wave. Meanwhile, in receptivity studies, both the discrete and continuous modes, including acoustic, entropy, and vorticity modes, contribute to the generation of the initial disturbance. The purpose of this paper is to introduce a new very high-order numerical method to accurately compute these normal modes with finite-difference on a non-uniform grid. Currently, numerical methods to obtain these normal modes include two major approaches, the boundary value problem approach and the initial value problem approach. The boundary value approach used by Malik (1990) [17] deploys fourth-order finite difference and spectral collocation methods to solve a boundary value problem for linear stability theory (LST). Nonetheless, Malik's presentation only demonstrated the computation of discrete modes, but not the continuous modes essential for conducting modal analysis on receptivity data. To obtain the continuous spectrum for his multimode decomposition framework, Tumin (2007) [16] relies on an initial value approach based on the Runge Kutta scheme with the Gram-Schmidt orthonormalization. However, the initial value approach is a local method that does not give a global evaluation of the eigenvalue spectra of discrete modes. Furthermore, Gram-Schmidt orthonormalization, which can be error-prone in implementation, is required at every step of the integration to minimize the accumulation of numerical errors. To overcome the drawbacks of these two approaches, this paper improves the boundary value approach by introducing a new general very high-order finite difference method for both discrete and continuous modes eigenfunctions. This general high-order finite difference method is based on a non-uniform grid method proposed by Zhong and Tatineni (2003) [22]. Under the finite difference framework, discrete and continuous modes can be obtained by imposing proper freestream asymptotic boundary conditions based on the freestream fundamental solution behavior. This asymptotic boundary condition is used for obtaining both discrete and continuous modes that have both distinct (acoustic) and similar (vorticity and entropy) eigenvalues. Extensive verification of the new method has been carried out by comparing the computed discrete and continuous modes. Subsequently, the discrete and continuous modes obtained with this finite difference method are essential for the bi-orthogonal decomposition, which holds promising potential in obtaining an accurate evaluation of receptivity coefficients. The result of the bi-orthogonal decomposition for a hypersonic boundary layer flow over a flat plate is verified by comparing with existing results. Ultimately, the bi-orthogonal decomposition

using the eigenfunctions has been applied to a case of freestream receptivity simulation for an axis-symmetric hypersonic flow over a blunt nose cone with modal contributions computed as coefficients for receptivity analysis.

1. Introduction

The precise prediction of laminar-to-turbulent transition within hypersonic boundary layers takes a significant role in the realm of aerodynamic design and control for hypersonic vehicles [1]. To understand the intricate transition behavior and maintain laminar flow, the study of boundary layer stability is divided into various paths depending on the disturbance, depicted by Morkovin [2]. In this paper, the main focus lies in the small initial disturbance regime. Due to a small perturbation, the disturbed flow experiences multiple stages comprised of receptivity, linear model growth, and nonlinear interaction breakdown leading to turbulence. During the receptivity process, a freestream pressure, entropy, or vorticity disturbance interacts with the boundary layer and generates the initial perturbations [3]. Fig. 1, adopted from He and Zhong [4], depicts the general receptivity process. As the disturbances enter the boundary layer, the reaction between the disturbance and the surface generates an initial instability which propagates downstream.

These weak initial disturbances undergo a progression marked by linear growth, subsequently leading to nonlinear interaction and energy exchange of modes [5]. The process of analyzing linear growth is commonly referred to as the linear stability theory (LST). Assuming the flow quantities to be composed of the base flow and the weak disturbance, the Navier-Stokes equations can be linearized and decomposed into various modes for analysis. Within the domain of LST, two categories of problems are being focused on, the temporal and spatial problems. The temporal problem refers to the variation of disturbance amplitude over time, leading to the computation of the complex frequency, ω. The spatial problem, on the other hand, refers to the amplitude changing with the spatial coordinate, which focuses the search on the complex wave number, α. The solutions for these two types of problems, temporal and spatial, are proven to contain a sum of discrete modes and continuous modes by Salwen and Grosch [6], and Tumin and Fedorov [7].

In this context, the discrete and continuous modes are the distinct eigenmodes to the linear stability problem. The discrete modes refer to the discrete normal modes computed by Mack [8] via LST. For instance, the first mode refers to the downstream growth of the Tollmien-Schlichting (T-S) waves. Moreover, the second mode and higher order modes discovered by Mack [8] (also denoted as the "Mack modes" or mode S/F defined by Fedorov and Tumin [9]) belong to a category of acoustic waves oscillate between the sonic point, where the velocity is equal to the local speed of sound, and the wall as depicted by Fedorov [10]. In addition to discrete modes, Mack [11] also investigated the possibility of the existence of a continuous spectrum of eigenvalues by investigating a plane Poiseuille flow and moving the upper plane to infinity. His calculations suggested that in addition to a finite number of discrete modes, a continuous spectrum of eigenvalues that lies along the phase velocity $c_r = 1$ exists. Continuing the investigation on the continuous modes, Salwen and Grosch [12] demonstrated that for an unbounded domain like the Blasius flow, the Orr-Sommerfield equation could require integration over a continuum in addition to discrete modes to construct a complete set of solution. They proved the existence of a continuous spectrum by relaxing the zero freestream boundary condition of the perturbations to have bounded magnitude. In essence, the continuous modes are not confined within the boundary layer but extend out to the freestream. From this result, Salwen and Grosch [6] continued to investigate and affirmed that the set of discrete and continuous modes of the temporal problem is complete. Thus, an expansion to the sum of discrete and continuous modes is needed to fully describe the temporal problem.

In the realm of spatial problem, Zhigulev, Sidorenko, and Tumin [13] proved that two continuous branches have upstream decaying modes, which correspond to a large growth rate in the downstream, from the incompressible Orr-Sommerfeld equations. Similarly, for the two-dimensional compressible spatial problem of two-dimensional perturbations, Tumin and Fedorov [7] revealed the existence of seven branches in the continuous spectrum with three being upstream propagating. This result suggested an ill-posedness situation of the spatial problem. In response to this problem, Tumin and Fedorov suggested a solution with a finite growth rate and proved that the remaining four branches formed a complete set of solutions in conjunction with the discrete modes. Therefore, a description of the spatial problem also includes both discrete and continuous modes. Let M be the Mach number, the continuous modes include a branch of the continuous fast acoustic wave that propagates at a relative phase speed of $1 + 1/M$ to the meanflow velocity, a branch of continuous slow acoustic wave at a relative phase speed of $1 - 1/M$, and two branches of entropy and vorticity waves which have the same phase velocity $c_r = 1$ as the meanflow. Furthermore, the discrete mode F originates from the branch of continuous fast acoustic while the discrete mode S is generated from the slow acoustic branch.

To numerically obtain these discrete and continuous modes, two approaches are commonly adopted by researchers, an initial value problem approach and a boundary value problem approach. Mack deployed the initial value problem approach with the Gram-Schmidt orthonormalization to integrate the inviscid solution from the freestream to the wall to obtain his discrete "Mack" modes. The same method is described by Scott and Watt [14] in detail. While computationally efficient, this method entails a cumbersome orthonormalization and recovery procedure at each step to minimize the numerical parasitic errors. A recovery process is also needed to scale the eigenfunctions properly. In addition, due to the non-linearity of the spatial problem, mainly in the $\frac{\partial^2}{\partial x^2}$ terms, Newton's method is deployed in the iteration to match the boundary condition at the wall. Following Mack, Tumin [15] also utilized the initial value problem approach to obtain both discrete and continuous eigenfunctions by integrating the freestream eigenfunction solutions to the wall in a two-dimensional incompressible boundary layer flow with a two-dimensional disturbance. Yet, to obtain the continuous modes, specific sets of freestream fundamental solutions are required for the integration towards the wall. This process of obtaining the linear combination of the fundamental solutions requires a complex Bromwich integral and an
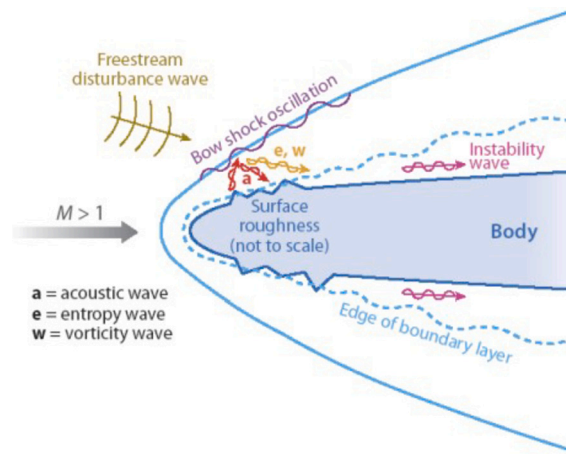
Fig. 1. Schematic diagram depicting general receptivity pathways, adopted from He and Zhong [4].

intricate algebraic manipulation [16]. This complex theoretical presentation of the continuous spectrum hinders the wide application of the bi-orthogonal decomposition. Furthermore, since the integration is for a wall-normal profile, this method is a local method that obtains the eigenmodes individually. Contrary to Mack, Malik [17] had formulated the spatial LST problem as a boundary value problem and separated the task into a global and local problem due to the non-linearity in the formulation of the spatial problem. This boundary value approach is often referred as to the LST method by researchers. The global method involves an eigendecomposition on the discrete operator assuming a linear relationship for the spatial eigenvalue α. With this assumption, the global method can closely approximate the whole spectrum of spatial eigenvalues. The local method, similar to Mack, utilizes Newton's method for a nonlinear iteration to converge on an eigenvalue that satisfies the boundary conditions. Malik employed a second-order (global eigenvalue decomposition) and fourth-order (local eigenvalue iteration) finite difference method as well as a spectral collocation method to perform the same task. While the spectral collocation offers a high order of accuracy, the linear operator is densely populated. Moreover, the LST method has also been applied widely in parallel with direct numerical simulations (DNS) to investigate disturbance behaviors in hypersonic flow [18], [19], [20]. In these studies, the boundary value approach result on LST has served as a direct comparison to the unsteady DNS result. Yet, Malik focused on the computation of discrete modes, and the uses of the LST as a comparison only focused on the unstable discrete modes.

Upon the above examination of the two approaches, it is evident that both numerical approaches exhibit certain limitations. The initial value approach, for instance, shows deficiencies including the locality of the method, the complex mathematical analysis, and the Gram-Schmidt orthonormalization, coupled with a complicated recovery process to scale the coefficient at each step after the integration. The locality of the method necessitates a precise initial guess to facilitate the convergence of the discrete mode eigenvalues. The complexity of the mathematical analysis to obtain the fundamental solution combination for each normal mode, characterized by intricate complex integrals, may pose challenges for engineering practitioners less familiar with advanced mathematical concepts. Moreover, both the orthonormalization and recovery process can be error-prone in the implementation, especially within the complex domain. In contrast to the initial value problem approach, the boundary value problem approach by Malik can be formulated into both global and local problems. The discrete operators for the boundary value problem approach are also straightforward to implement. Nevertheless, despite the advantages, Malik has only demonstrated the computation of discrete modes.

To address the limitations of the numerical approaches, the boundary value problem approach can be revisited on the computation of continuous spectrum eigenfunctions. In this work, a new very high-order finite difference scheme is introduced to compute both discrete and continuous modes. While Malik's work primarily presented lower-order finite difference methods and a high-cost spectral collocation method, this paper explores the potential of a high-order finite difference scheme over a non-uniform grid for the computation of both discrete and continuous modes. In particular, high-order finite difference methods have already been applied in various direct numerical simulation (DNS) studies. Zhong [21] developed high-order (up to 16th-order) finite difference schemes with non-uniform grid direct discretization for the computation of compressible boundary layer flow based on the full nonlinear Navier-Stokes equations, which can be adopted in the linear stability problem as well. A more extensive presentation of the family of high-order finite difference schemes can also be found in Zhong and Tatineni [22]. Furthermore, Shukla, Tatineni, and Zhong [23] later extended the use of these finite difference schemes in the incompressible flow regime. In addition to the use of finite difference schemes in DNS, Mortensen and Zhong [24] introduced the use of Lagrange polynomials to develop a high-order finite difference method as an extension to Malik's LST formulation [17] for computing discrete modes. The current work builds upon this foundation, exploring the extension of the finite difference method to efficiently compute the continuous modes, thus providing accuracy and computational efficiency.

In addition to the computation of eigenfunctions, Tumin also implemented the bi-orthogonality condition first described by Salwen and Grosch [6] to develop a bi-orthogonal eigenfunction system for flowfield decomposition in the regime of incompressible flow [15]. This bi-orthogonal eigenfunction system introduces an adjoint formulation of the direct LST problem, establishing an orthogonality relation between distinct normal modes. Using this orthogonality relation, this bi-orthogonal decomposition can be

applied to both temporal and spatial problems allowing the decomposition of a disturbance flowfield into discrete and continuous modes. Subsequently, Gaydos and Tumin also extended the scope of the study to a two-dimensional compressible case with two-dimensional disturbance [25]. In addition, Tumin considered a three-dimensional disturbance on a two-dimensional compressible boundary layer [16] and developed the bi-orthogonal eigenfunction system for the two-dimensional compressible boundary layer problem. With the bi-orthogonal eigenfunction system, it is possible to investigate the instability of hypersonic boundary layers systematically for a better understanding of the physics of the flow.

Moreover, precise evaluation of the bi-orthogonal eigenfunction system holds substantial promise for enhancing existing transition prediction techniques. Notably, the widely employed e^N method revolves around the assessment of the growth of discrete normal modes, typically determined through the application of LST or DNS. Furthermore, the incorporation of bi-orthogonal decomposition assumes a significant role in the investigation of freestream receptivity of hypersonic flow, capable of providing a more comprehensive interpretation of the primary origins of disturbances. The current state-of-the-art transition prediction amplitude method by Mack [26] relies on an accurate initial disturbance amplitude, or so-called receptivity coefficient, to predict the transition location. Presently, the receptivity coefficient is obtained either empirically by correlation such as in Marineau's work [27] or through a combination of LST and DNS results suggested by Huang and Zhong [28]. The computational approach for obtaining the receptivity coefficient is an approximated approach that obtains the initial amplitude by dividing the disturbance amplitude at a later location where the unstable mode is dominant with the N factor growth rate of the unstable mode [19]. Since only the second mode is present in the downstream region where the second mode assumes dominance, this reverse technique is proven to be effective. Yet, the direct evaluation of the initial perturbation at the branch I neutral stability point, where the instability starts on the neutral curve, is still an active area of research. Given that the initial disturbance can entail weak contributions from various modes, the application of bi-orthogonal decomposition holds particular promise. A survey of applications to receptivity problems in computational and experimental work can also be found in reference [29]. Saikia et al. [30] used the bi-orthogonal eigenfunction system to examine the amplification of the hypersonic discrete mode of a high enthalpy flow over a flat plate. Hasnine et al. [31] [32] studied a particulate-induced disturbance over a plate boundary layer of a high-speed flow by decomposing the unsteady flowfield with discrete modes S and F as well as continuous fast and slow acoustic modes. Tumin et al. [33] and Miselis [34] applied the bi-orthogonal eigenfunction system for a freestream hotspot receptivity study of hypersonic flow over a wedge geometry for the consideration of weakly non-parallel flow. Yet, the bi-orthogonal decomposition applications of DNS data for broadband freestream disturbances to obtain receptivity coefficients are limited [4]. To further the progress in the bi-orthogonal decomposition application for receptivity studies, a systematic approach for computing the discrete and continuous modes with high accuracy and efficiency is necessary. Thus, this paper also encompasses an example of the bi-orthogonal decomposition using the newly computed eigenfunction result for demonstration purposes.

Moreover, input-output or resolvent analysis is another popular tool for transition analysis. In the input-output approach, the Navier-Stokes equations are discretized, using spectral collocation method [35], [36], finite volume method [37] or a numerical Jacobian method by extracting the linear operator from known solvers [38] [39]. An arbitrary forcing, including the nonlinear term from the full nonlinear Navier-Stokes equation [35] [40] or an external forcing on the linearized Navier-Stokes equations [36] [37] [38], acts as the input to the discrete operator and the response of the forcing is studied. Although this analysis accounts for the non-modal effects, both full singular value decomposition (SVD) of the resolvent operator and the popular power iteration method only decomposes disturbances into modes with respect to the energy norm presented by Chu [41]. This can be less informative than the bi-orthogonal decomposition which decomposes the perturbed flowfield into modes according to physical interpretation including acoustic, entropy, and vorticity modes. Moreover, with contributions of different modes known, non-modal effects can also be accounted for in the bi-orthogonal eigenfunction decomposition.

In this work, the goal is to develop a new method for obtaining both discrete and continuous modes using very high-order finite differences on a non-uniform grid in the application of bi-orthogonal decomposition. The first part of the paper will be focused on reformulating the boundary value problem approach for the continuous spectra while maintaining the mathematical rigor of Tumin's work [16]. The part will start with a presentation of the governing equations and the formulation of the spatial problem in section 2. Then the linear combination of the freestream asymptotic fundamental solutions to obtain the continuous modes will be revisited by inspecting the physical behavior of each continuous mode. These combinations will be presented without the complex Bromwich integral and manipulation. The orthogonality between each normal mode will serve as a validation tool to maintain the mathematical rigor for the reformulation. In Section 3, the finite difference numerical method is then formulated for obtaining both the discrete and the continuous modes. The very high-order finite difference scheme on a non-uniform grid allows the high-order and stable computation of the bi-orthogonal eigenfunction system while keeping the sparse structure for efficiency. Applying the asymptotic fundamental solutions as freestream boundary conditions, the complete set of discrete and continuous spectra can be obtained.

The new high-order method is verified by comparing the computed discrete and continuous modes with various cases of hypersonic flow over a flat plate from Tumin [16] and Miselis [34]. The bi-orthogonal decomposition for the flat plate case is performed to demonstrate the bi-orthogonal relationship. Furthermore, the bi-orthogonal eigenfunction system is presented for a Mach 9.81 hypersonic flow over a 5.08 *mm* nose radius blunt cone from He and Zhong [19]. Finally, the bi-orthogonal decomposition is applied on the unsteady DNS flowfield of a freestream receptivity simulation for the same flow to obtain the contribution amplitude of each mode including discrete and continuous modes for future receptivity coefficient calculation.

2. Governing equations

2.1. Navier-Stokes equations

The Navier-Stokes equations for a viscous compressible flow of ideal gas in Cartesian Coordinates are

$$\frac{\partial \rho^*}{\partial t^*} = \nabla^* \cdot \left(\rho^* \mathbf{u}^* \right) = 0 \tag{1}$$

$$\rho^* \left[\frac{\partial \mathbf{u}^*}{\partial t^*} + \left(\mathbf{u}^* \cdot \nabla^* \right) \mathbf{u}^* \right] = -\nabla^* p^* + \nabla^* \cdot \left[\lambda^* \left(\nabla^* \cdot u^* \right) \mathbf{I} + \mu^* \left(\nabla^* \mathbf{u}^* + \nabla^* \mathbf{u}^{*T} \right) \right] \tag{2}$$

$$\rho^* c_p^* \left[\frac{\partial T^*}{\partial t^*} + \left(\mathbf{u}^* \cdot \nabla^* \right) T^* \right] = -\nabla^* \cdot \left(\kappa^* \nabla^* T^* \right) + \frac{\partial p^*}{\partial t^*} + \mathbf{u}^* \cdot \nabla^* p^* + \Phi^* \tag{3}$$

where viscous dissipation function is

$$\Phi^* = \lambda^* \left(\nabla^* \cdot \mathbf{u}^* \right)^2 + \frac{\mu^*}{2} \left[\nabla^* \mathbf{u}^* + \nabla^* \mathbf{u}^{*T} \right]^2. \tag{4}$$

The ideal gas law is expressed as

$$p^* = \rho^* R^* T^*. \tag{5}$$

In the above equations, the asterisk, $*$, represents the dimensional form of the variables. The coefficient, c_p is the specific heat, and κ is the heat conductivity. We also make use of the Stokes' hypothesis of $\lambda^* = -2\mu^*/3$. The viscosity μ is given by the Sutherland formula.

$$\mu = \mu_{ref} \left(\frac{T}{T_{ref}} \right)^{3/2} \frac{T_{ref} + S_\mu}{T + S_\mu}. \tag{6}$$

The thermal conductivity k may also be formulated by the Sutherland formula with the Sutherland temperature S_k. For the result of this paper, however, k is computed by assuming a Prandtl number $Pr = 0.72$, defined as $\mu c_p / k$ where c_p is the specific heat at constant pressure and assumes constant for a perfect gas.

2.2. Compressible linear stability equations

From the Navier-Stokes equations, we can derive the stability equations by assuming a small disturbance added on to the quantities.

$$\begin{aligned} &u = \bar{U} + \tilde{u}, \;\; v = \bar{V} + \tilde{v}, \;\; w = \bar{W} + \tilde{w} \\ &p = \bar{P} + \tilde{p}, \;\; \tau = \bar{T} + \tilde{\theta}, \quad \rho = \bar{\rho} + \tilde{\rho} \\ &\mu = \bar{\mu} + \tilde{\mu}. \end{aligned} \tag{7}$$

Here, the "bar" quantities represent the mean variables, and the "bar" symbol is dropped in the following formulation for simplicity. All flow variables are scaled by their corresponding boundary layer edge values and a reference length scale L is assumed. By applying the local parallel flow assumption and subtracting the base flow equations, we can obtain the non-dimensional linear stability equations that can be found in various previous works [16] [34] [42]. With the above assumption of small perturbations, the higher-order terms after the substitution can be dropped. Hence, the governing equations are linearized. For a flat plate profile, the assumption of $dP/dy \to 0$ causes the pressure profile to be constant, $P = 1/\gamma M_\infty^2$. For meanflow profiles of other geometry, as suggested by Miselis [34], the assumption is not applicable and the meanflow pressure distribution has to be accounted for in the linearized equations. Moreover, the meanflow temperature boundary condition can be adiabatic or heat transfer at the wall while the fluctuation temperature boundary condition is set to be zero on the wall. This is under an assumption due to the small disturbance and thermal inertia of the wall. The no-slip condition at the wall also applies.

$$y = 0: \quad u, v, w, \theta = 0. \tag{8}$$

Thus, four physical boundary conditions exist at the wall. In the next section, the disturbance will take the form of a propagating wave and the spatial Cauchy problem will be set up.

2.3. Spatial Cauchy problem

Following [16], a three-dimensional spatially growing perturbation is considered in a boundary layer flow. From the above linearized Navier-Stokes equations, we can assume a periodic-in-time perturbation with a non-dimensional circular frequency ω that leads to a solution as $\exp(-i\omega t)$ after a Fourier transformation in time is performed. For clarity purposes, the relation between the dimensional and non-dimensional frequencies is listed as follows, where $*$ denotes the dimensional variable.

$$\omega = \frac{\omega^* L^*}{u_\infty^*}, \quad F = \frac{2\pi f^* \mu_\infty^*}{\rho_\infty^* u_\infty^{*2}} = \frac{\omega^* \mu_\infty^*}{\rho_\infty^* u_\infty^{*2}} \tag{9}$$

where f^* is the dimensional frequency in hertz. The local Reynolds number and the reference boundary layer thickness L^* are formulated as

$$R = \frac{\rho_\infty^* u_\infty^* L^*}{\mu_\infty^*}, \quad L^* = \sqrt{\frac{\mu_\infty^* x^*}{\rho_\infty^* u_\infty^*}} \tag{10}$$

Following Tumin [16], the linearized Navier-Stokes system can be rewritten in the following form,

$$\frac{\partial}{\partial y}\left(\mathbf{L}_0 \frac{\partial \mathbf{A}}{\partial y}\right) + \mathbf{L}_1 \frac{\partial \mathbf{A}}{\partial y} = \mathbf{H}_1 A + \mathbf{H}_2 \frac{\partial \mathbf{A}}{\partial x} + \mathbf{H}_3 \frac{\partial \mathbf{A}}{\partial z} + \mathbf{F} \tag{11}$$

where $\mathbf{L}_0$, $\mathbf{L}_1$, $\mathbf{H}_1$, $\mathbf{H}_2$, and $\mathbf{H}_3$ are 16 by 16 matrices of coefficients. Since these coefficient matrices are not required for the implementation, refer to [16] for the non-zero entries. Furthermore, $\mathbf{F}$ above denotes the initial data of $\mathbf{H}_2\mathbf{A}_0$ at $x = 0$. The perturbation variables are defined in a column vector $\mathbf{A}$ with 16 components. For simplicity purposes, the tilde on perturbation variables such as $\tilde{u}$ is dropped and u will be used.

$$\mathbf{A}(x, y, z) = (u, \partial u/\partial y, v, \pi, \theta, \partial \theta/\partial y, w, \partial w/\partial y, \partial u/\partial x, \partial v/\partial x$$
$$\partial \theta/\partial x, \partial w/\partial x, \partial u/\partial z, \partial v/\partial z, \partial \theta/\partial z, \partial w/\partial z)^T. \tag{12}$$

To analyze the spatial growth rate, we apply a Laplace transform in the x direction and a Fourier transform in the z direction assuming spanwise periodic perturbation.

$$\mathbf{A}_{\alpha\beta} = \int_0^\infty e^{-i\alpha x} \int_{-\infty}^\infty e^{-i\beta z} \mathbf{A}(x, y, z) \, dz \, dx, \tag{13}$$

where α is the spatial eigenvalue of interest. After the transformations, the system can be written as

$$\frac{\partial}{\partial y}\left(\mathbf{L}_0 \frac{\partial \mathbf{A}_{\alpha\beta}}{\partial y}\right) + \mathbf{L}_1 \frac{\partial \mathbf{A}_{\alpha\beta}}{\partial y} = \mathbf{H}_1 \mathbf{A}_{\alpha\beta} + i\alpha \mathbf{H}_2 \mathbf{A}_{\alpha\beta} + i\beta \mathbf{H}_3 \mathbf{A}_{\alpha\beta} + \mathbf{H}_2 \mathbf{A}_{0\beta}$$
$$y = 0: (\mathbf{A}_{\alpha\beta})_k = 0, \quad k = 1, 3, 5, 7$$
$$y \to \infty: \left|(\mathbf{A}_{\alpha\beta})_k\right| < \infty, \quad k = 1, \cdots, 16, \tag{14}$$

with $(\mathbf{A}_{\alpha\beta})_k$ being the kth component of the vector. Note that the wall boundary conditions presented do not apply to cases with wall blowing or suction. The homogeneous part of Eq. (14) can be recast as a first-order system of eight components of the following by substituting the continuity equation into y direction momentum equation,

$$\frac{d\mathbf{z}_{\alpha\beta}}{dy} = \mathbf{H}\mathbf{z}_{\alpha\beta}$$
$$y = 0: (\mathbf{z}_{\alpha\beta})_k = 0, \quad k = 1, 3, 5, 7$$
$$y \to \infty: \left|(\mathbf{z}_{\alpha\beta})_k\right| < \infty, \quad k = 1, \cdots, 8, \tag{15}$$

where $\mathbf{z}_{\alpha\beta}$ is defined as

$$\mathbf{z}_{\alpha\beta} = (u, \partial u/\partial y, v, \pi, \theta, \partial \theta/\partial y, w, \partial w/\partial y). \tag{16}$$

Here, $\mathbf{H}$ is a 8 by 8 coefficient matrix. The elements of $\mathbf{H}$ can be found in Appendix A. In the implementation of the bi-orthogonal decomposition, the reduced system is solved numerically instead of the large system of Eq. (14). However, the system in Eq. (14) is necessary to introduce the adjoint system. The fundamental solution to Eq. (15) can be written as the following with the reduced system,

$$\mathbf{z}_{\alpha\beta}(y) = \mathbf{z}_{\alpha\beta}^{(\mathbf{m})}(y) c^{(m)}(y) \quad m = 1, \cdots, 8, \tag{17}$$

with complex coefficients $c^{(m)}$ for the mth fundamental solution. Each fundamental solution $\mathbf{z}_{\alpha\beta}^{(\mathbf{m})}(y)$, $m = 1, \cdots, 8$ satisfies the following

$$\frac{d\mathbf{z}_{\alpha\beta}^{(\mathbf{m})}}{dy} = \mathbf{H}\mathbf{z}_{\alpha\beta}^{(\mathbf{m})}(y), \quad m = 1, \cdots, 8. \tag{18}$$

Note that the boundary conditions of Eq. (15) do not transcribe to Eq. (18) directly. The wall boundary conditions will be satisfied in the determination of the coefficients $c^{(m)}$ in the linear combination. Since the matrix $\mathbf{H}$ from Eq. (18) is a matrix of constant coefficients in the region outside of the boundary layer, the asymptotic solutions to Eq. (18) take the form of

$$y \to \infty: \mathbf{z}_{\alpha\beta}^{(\mathbf{m})}(y) = \mathbf{z}_{\alpha\beta_0}^{(\mathbf{m})} e^{\lambda_m y}, \quad m = 1, \cdots, 8. \tag{19}$$

where $\mathbf{z}_{\alpha\beta_0}^{(m)}$ is the mth freestream fundamental solution, which can be solved from the following characteristic equation,
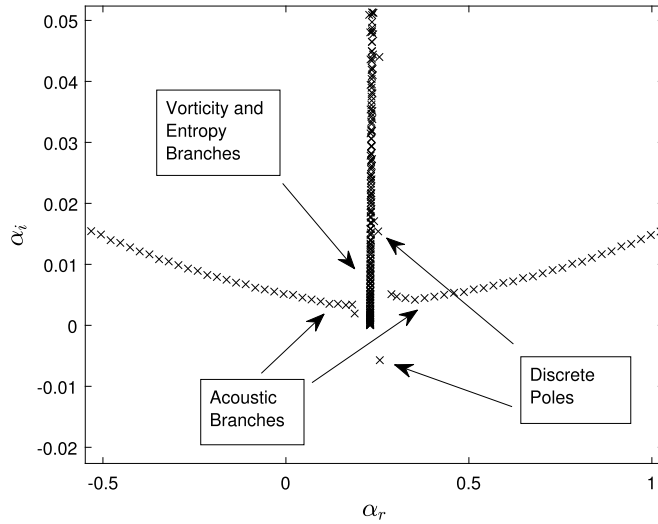
Fig. 2. The global spatial eigenvalue spectrum showing the continuous branch cuts and discrete poles.

$$\left(\mathbf{H} - \lambda_m \mathbf{I} \right) \mathbf{z}_{\alpha\beta_0}^{(\mathbf{m})} = 0, \quad m = 1, \cdots, 8. \tag{20}$$

The eigenvalues λ_m and the corresponding asymptotic solutions $\mathbf{z}_{\alpha\beta_0}^{(\mathbf{m})}$ are presented in Appendix B and can also be found in the existing work of Tumin [16]. The eigenvalue λ_m is a function of α on the complex α plane. A total of eight fundamental solutions exist with four solutions having the asymptotic behavior of $\sim \exp(\lambda_m y)$, $m = 2$, 4, 6, 8 where $Re(\lambda_m) > 0$ and the other four solutions being $\sim \exp(\lambda_m y)$, $m = 1$, 3, 5, 7 where $Re(\lambda_m) < 0$ for a complex λ_m value. This corresponds to the discrete modes discussed in the previous section which can be represented with the four $\sim \exp(\lambda_m y)$, $m = 1$, 3, 5, 7 decaying solutions to satisfy the zero freestream boundary condition. Hence, an additional iteration for α is required to satisfy four physical wall boundary conditions and one additional normalizing condition to specify a particular mode.

For an oscillating continuous mode, on the other hand, the eigenvalues for the mth branch are imposed to have $Re(\lambda_m(\alpha)) = 0$ with the branch parameter K,

$$\lambda_m(\alpha)^2 = -K^2, \tag{21}$$

for a real valued $K > 0$ for their corresponding $\lambda_m(\alpha)$ along the mth branch cut. Since λ is the eigenvalue in the wall-normal direction, the parameter K can also be interpreted as the wavenumber in the wall-normal direction. The discrete α values of a sample compressible flow over a flat plate are plotted in Fig. 2 to show the branches and poles on the complex α plane. A discrete representation of the continuous branch cuts is presented since each branch can be described with the wall-normal wavenumber K for a range of discrete values from 0 to ∞. Further discussion on the formulation of both discrete and continuous modes will follow.

2.4. Discrete modes

The discrete modes, shown as poles in the complex α plane, are freestream decaying modes including mode F, originating from the fast acoustic spectrum, mode S, originating from the slow acoustic spectrum and higher order modes [5]. Physically, they are the decaying TS waves and trapped acoustics waves inside the boundary layer. For discrete modes, the boundary condition at the freestream can be formulated as a decaying condition in addition to the bounded condition in Eq. (15). From the asymptotic fundamental solutions, a total of eight fundamental solutions exist with four solutions having the asymptotic behavior of $\sim \exp(\lambda_m y)$, $m = 2$, 4, 6, 8 where $Re(\lambda_m) > 0$ and the other four solutions being $\sim \exp(\lambda_m y)$, $m = 1$, 3, 5, 7 where $Re(\lambda_m) < 0$. The discrete modes were shown by Tumin to be a combination of the decaying fundamental solutions with $Re(\lambda_m) < 0$ [16]. Based on the decaying nature of these fundamental solutions in freestream, the freestream boundary conditions can also be written as

$$y \to \infty : (\mathbf{z}_{\alpha\beta})_k = 0, \quad k = 1, \cdots, 8. \tag{22}$$

These freestream boundary conditions can replace the freestream boundary conditions in Eq. (15) and form a homogeneous problem. Thus, for discrete modes, the problem takes the form of a nonlinear eigenvalue problem where the eigenfunctions represent the wave shape and the eigenvalues represent the complex streamwise wavenumber, α, in the flowfield. Since the complex streamwise wavenumber α acts as an eigenvalue for the system, a negative imaginary part of α indicates flow instability. Furthermore, the individual fundamental solutions defined by Eq. (17) do not need to be solved as the solutions to this homogeneous problem are the discrete mode eigenfunctions. This homogeneous problem, however, always includes a trivial solution due to the zero boundary conditions at both the wall and the freestream. To avoid this trivial solution, the same problem can be formulated into a boundary value problem with an additional wall boundary condition of wall pressure normalization,

$$(\mathbf{z}_{\alpha\beta}(y=0))_4 = p_w(\alpha) = 1. \tag{23}$$

where $p_w(\alpha)$ denotes the wall pressure as a function of the streamwise wavenumber α. The problem now becomes a non-homogeneous boundary value problem as a non-linear function of the streamwise wavenumber α. To obtain the correct α to satisfy the boundary conditions, the problem can be solved with a non-linear iterative scheme such as Newton's iteration. This process will be discussed further in a later section.

2.5. Continuous spectra

In addition to the discrete modes, the solution $\mathbf{A}_{\alpha\beta}$ also contains continuous modes which are the neutral oscillating waves allowed by the boundedness freestream condition. This boundedness condition can be represented with the freestream fundamental solutions for each continuous branch by imposing Eq. (21) where the wavenumber K is a positive real number. Since four pairs of λ exist, four types of continuous modes are used to describe the different roots of λ. For the pair of λ_m, where $m = 1, 2$, the corresponding eigenfunctions represent the spanwise vorticity disturbances, whereas $m = 7, 8$ represent the streamwise vorticity disturbances at the freestream. For the acoustic and entropy modes, the nonzero components of these eigenvectors are presented as $(\mathbf{z}_{\alpha\beta_0}^{(\mathbf{m})})$ for $m = 3, 4, 5, 6$ being the mth eigenvector shown in Appendix B. From the eigenfunctions, the acoustics and entropy branches cannot be characterized directly. Yet, when the equation $\lambda(\alpha)_m^2 = -K^2$, $m = 3, 4, 5, 6$ is solved, the phase speed c_r can be calculated from the spanwise wavenumber α. For a two-dimensional disturbance, $\beta = 0$, the phase speed of the disturbance can be calculated as

$$c_r = \frac{\omega}{\alpha_r}, \tag{24}$$

with α_r being the real part of the wavenumber. For acoustics modes, two acoustic modes exist with one traveling at the phase speed of $c_r = 1 + 1/M_\infty$ and the other at $c_r = 1 - 1/M_\infty$. These are referred to as the fast and slow acoustic continuous spectra. The entropy mode, on the other hand, travels with the same speed as the meanflow, $c_r = 1$. From the phase speeds, the pair $m = 3, 4$ represents the acoustics modes, and $m = 5, 6$ represents the entropy mode. From the freestream fundamental solutions, the dominating eigenpairs are determined for each continuous mode. Yet, looking at Fig. 2, the vorticity and entropy branches overlap especially in the region near the branch point of each branch. Hence, the freestream behavior of these continuous modes is influenced by the others in the same region. When Eq. (21) is solved for $m = 1, 2, 5, 6, 7, 8$, the wavenumber α is very close to the other branches in the overlapping region, causing the corresponding fundamental solutions to be non-decaying as well. Hence, the influence of the other non-decaying solutions in addition to the dominating fundamental solutions needs to be accounted for. In the upcoming section, the continuous branches in both isolated and overlapping regions will be formulated.

2.5.1. Acoustic modes

The acoustic branches correspond to the two isolated α branches extending in the α_r direction in Fig. 2. Depending on the wavenumber and its corresponding phase speed, the slow or fast acoustic branch can be selected. These two branches have the dominating fundamental solutions being the $m = 3, 4$ fundamental solutions which are primarily outgoing and incoming acoustic waves. Thus, the solution of Eq. (15) at the freestream can be expressed as incoming and outgoing acoustic waves using the fundamental solutions $\mathbf{z}_{\alpha\beta_0}$,

$$y \to \infty : \mathbf{z}_{\alpha\beta} = c^{(3)}\mathbf{z}_{\alpha\beta_0}^{(\mathbf{3})} + c^{(4)}\mathbf{z}_{\alpha\beta_0}^{(\mathbf{4})}. \tag{25}$$

Since a total of four wall boundary conditions and a normalizing condition have to be satisfied, the three decaying fundamental solutions from the rest of the pairs of fundamental solutions will be used in the linear combination. Thus, the following combination,

$$\mathbf{z}_{\alpha\beta}^{AC} = c^{(3)}\mathbf{z}_{\alpha\beta}^{(3)} + c^{(4)}\mathbf{z}_{\alpha\beta}^{(4)} + c^{(1)}\mathbf{z}_{\alpha\beta}^{(1)} + c^{(5)}\mathbf{z}_{\alpha\beta}^{(5)} + c^{(7)}\mathbf{z}_{\alpha\beta}^{(7)}, \tag{26}$$

is obtained for the fast and slow acoustic modes. In this paper, the following notation is used to represent the five fundamental solution combinations for each mode. For example, the combination (1-3-4-5-7) represents the combination of fundamental solutions used for the acoustic modes. While Tumin had also solved the inverse Fourier transform for Eq. (14) analytically and verified the symbolic solution with the help of *Mathematica* [16], the fundamental solution combinations are plotted in this paper to showcase the physical behavior for clarity. Hence, five fundamental solutions are solved by using the asymptotic fundamental solutions as freestream boundary conditions,

$$\frac{\partial \mathbf{z}_{\alpha\beta}^{(\mathbf{m})}}{\partial y} = \mathbf{H}\mathbf{z}_{\alpha\beta}^{(\mathbf{m})}, \quad m = 1, 3, 4, 5, 7$$

$$y \to \infty : \mathbf{z}_{\alpha\beta}^{(\mathbf{m})} = \mathbf{z}_{\alpha\beta_0}^{(\mathbf{m})}, \quad m = 1, 3, 4, 5, 7. \tag{27}$$

Note that the set of freestream fundamental solutions $\mathbf{z}_{\alpha\beta_0}^{(\mathbf{m})}$ are the asymptotic solutions of the fundamental solutions. In addition, the freestream boundary conditions can be applied at the boundary layer edge or a further distance in the freestream. It is shown in the result section that the eigenfunction obtained by applying the boundary conditions behind the shock is equivalent to applying at the boundary layer edge. Furthermore, the wall boundary conditions are not imposed when the fundamental solutions are solved.

Eq. (27) is solved five times to obtain the five fundamental solutions. The coefficients $c^{(m)}$, $m = 1, 3, 4, 5, 7$, are determined uniquely with the four physical boundary conditions from Eq. (15) and one normalizing condition, $p = 1$, at the wall.

$$
\begin{bmatrix} u \\ \frac{du}{dy} \\ v \\ p \\ \theta \\ \frac{d\theta}{dy} \\ w \\ \frac{dw}{dy} \end{bmatrix} = \begin{bmatrix} 0 \\ \frac{du}{dy} \\ 0 \\ 1 \\ 0 \\ \frac{d\theta}{dy} \\ 0 \\ \frac{dw}{dy} \end{bmatrix} = \left[\mathbf{z}_{\alpha\beta}^{(1)}, \mathbf{z}_{\alpha\beta}^{(3)}, \mathbf{z}_{\alpha\beta}^{(4)}, \mathbf{z}_{\alpha\beta}^{(5)}, \mathbf{z}_{\alpha\beta}^{(7)} \right] \begin{bmatrix} c^{(1)} \\ c^{(3)} \\ c^{(4)} \\ c^{(5)} \\ c^{(7)} \end{bmatrix}
\tag{28}
$$

where rows 1, 3, 4, 5, 7 can be used to solve for the five coefficients, $c^{(m)}$, $m = 1, 3, 4, 5, 7$. After solving for the coefficients, Eq. (26) is applied to obtain the corresponding continuous acoustic mode. The selection of the normalizing condition can be varied to suit the needs of the problem. For example, one also can set the normalizing constant at the freestream to introduce an acoustic wave impinging the boundary layer. If this condition was imposed, the pressure at the wall would be solved as a part of the solution. Note that the same normalizing condition has to be applied for all eigenfunctions during the bi-orthogonal decomposition. For this paper, the normalizing constant is the pressure at the wall for demonstration.

2.5.2. Overlapping vorticity modes

For the case of hypersonic perturbation, Tumin [16] had demonstrated two overlapping behaviors of the vorticity and entropy modes. In the vicinity of the branch point, the vorticity and entropy branches are overlapping since the wavenumber α approaches proximity. In the limit of large α, the entropy mode diverges from the two vorticity modes. Consequently, the focus of the section first centers on the overlapping region characterized exclusively by the two vorticity modes with their fundamental solutions indexed $m = 1, 2, 7, 8$.

Due to the repeated eigenvalue pairs $\lambda_{1,2} = \lambda_{7,8}$, the two vorticity modes always overlap. Within this overlapping region, the spanwise vorticity mode contains the pair of asymptotic solutions, $\mathbf{z}_{\alpha\beta_0}^{(1)}$ and $\mathbf{z}_{\alpha\beta_0}^{(2)}$ corresponding to the incoming and outgoing spanwise vorticity, along with a contribution from the other overlapping branch. Similarly, the streamwise vorticity mode is dominated by the pair of asymptotic solutions, $\mathbf{z}_{\alpha\beta_0}^{(7)}$ and $\mathbf{z}_{\alpha\beta_0}^{(8)}$ corresponding to streamwise vorticity waves. To obtain two modes that are orthogonal to each other through the bi-orthogonality relation, which will be discussed later, only one fundamental solution from the other overlapping branch is considered in addition to the dominating fundamental solutions. This is equivalent to setting one incoming or outgoing vorticity wave to be zero at the freestream. Thus, for the first vorticity mode with $\lambda_{1,2}$, which corresponds to the spanwise vorticity perturbation, two freestream combinations containing three non-decaying fundamental solutions can be obtained

$$
y \to \infty : \mathbf{z}_{\alpha\beta} = c^{(1)} \mathbf{z}_{\alpha\beta_0}^{(1)} + c^{(2)} \mathbf{z}_{\alpha\beta_0}^{(2)} + c^{(7)} \mathbf{z}_{\alpha\beta_0}^{(7)},
\tag{29}
$$

or

$$
y \to \infty : \mathbf{z}_{\alpha\beta} = c^{(1)} \mathbf{z}_{\alpha\beta_0}^{(1)} + c^{(2)} \mathbf{z}_{\alpha\beta_0}^{(2)} + c^{(8)} \mathbf{z}_{\alpha\beta_0}^{(8)}.
\tag{30}
$$

To determine the correct combination, the physical behavior of the eigenfunction is examined. Specifically, for the spanwise vorticity mode, the solution should have a minimum streamwise vorticity as indicated in Eq. (84). Hence, the spanwise and streamwise vorticity components are compared in the result section. Accounting for both the decaying and non-decaying modes, two combinations of five fundamental solutions exist, (1-2-3-5-7) and (1-2-3-5-8). Shown in the later result section, the combination (1-2-3-5-7) demonstrates a reduced streamwise vorticity magnitude while retaining an equivalent spanwise vorticity magnitude as the alternative combination. This comparative result is presented in the later section on numerical results. Further validation of the numerical rigor for this combination is also undertaken with the bi-orthogonality relation, which is presented in the subsequent section. Additionally, upon solving Eq. (21) for $m = 1, 2$ to obtain the wavenumber α, two α values corresponding to the upstream and downstream propagating waves exist. However, only the downstream propagating disturbance wave is considered physical in this case. Similarly to the acoustic modes, a total of five fundamental solutions are needed to satisfy the five wall boundary conditions. Combining the decaying modes, the following combination, denoted as (1-2-3-5-7), is constructed to represent the spanwise vorticity mode,

$$
\mathbf{z}_{\alpha\beta}^{VA} = c^{(1)} \mathbf{z}_{\alpha\beta}^{(1)} + c^{(2)} \mathbf{z}_{\alpha\beta}^{(2)} + c^{(3)} \mathbf{z}_{\alpha\beta}^{(3)} + c^{(5)} \mathbf{z}_{\alpha\beta}^{(5)} + c^{(7)} \mathbf{z}_{\alpha\beta}^{(7)}.
\tag{31}
$$

Each 8-component fundamental solution can be determined as

$$
\frac{\partial \mathbf{z}_{\alpha\beta}^{(m)}}{\partial y} = \mathbf{H} \mathbf{z}_{\alpha\beta}^{(m)}, \quad m = 1, 2, 3, 5, 7
$$
$$
y \to \infty : \mathbf{z}_{\alpha\beta}^{(m)} = \mathbf{z}_{\alpha\beta_0}^{(m)}, \quad m = 1, 2, 3, 5, 7.
\tag{32}
$$

To be consistent, five fundamental solutions $\mathbf{z}_{\alpha\beta_0}^{(m)}$, $m = 1, 2, 3, 5, 7$ are solved for the spanwise vorticity mode (VA). Hence, the five coefficients $c^{(m)}$, $m = 1, 2, 3, 5, 7$ are determined uniquely with the normalization of wall pressure and the other four physical boundary conditions in the same fashion as Eq. (28). The above formulation can be easily implemented and solved numerically in practice. For the streamwise vorticity modes, similar to the spanwise counterpart, two combinations also exist. With the dominating fundamental solution being $\mathbf{z}_{\alpha\beta}^{(7)}$ and $\mathbf{z}_{\alpha\beta}^{(8)}$, the asymptotic behavior of the streamwise vorticity modes can be characterized as one of the following,

$$y \to \infty : \mathbf{z}_{\alpha\beta} = c^{(7)}\mathbf{z}_{\alpha\beta_0}^{(7)} + c^{(8)}\mathbf{z}_{\alpha\beta_0}^{(8)} + c^{(1)}\mathbf{z}_{\alpha\beta_0}^{(1)}, \tag{33}$$

or

$$y \to \infty : \mathbf{z}_{\alpha\beta} = c^{(7)}\mathbf{z}_{\alpha\beta_0}^{(7)} + c^{(8)}\mathbf{z}_{\alpha\beta_0}^{(8)} + c^{(2)}\mathbf{z}_{\alpha\beta_0}^{(2)}. \tag{34}$$

Similarly, one can inspect the vorticity components and find that the combination (2-3-5-7-8), where the third and fifth fundamental solutions are decaying, has a larger streamwise vorticity component. Each fundamental solution and its corresponding equations can be determined in a similar formulation as the spanwise vorticity mode. Furthermore, the bi-orthogonality of the resulting modes will be validated numerically using the bi-orthogonal relation in the later section.

2.5.3. Overlapping entropy mode

After obtaining the vorticity modes, the determination of the entropy mode proceeds by examining the overlapping region near the branch point. In this overlapping region of the complex α plane, two vorticity modes and one entropy mode interact with each other. Since the dominating fundamental solution of the entropy mode will be the 5th and 6th fundamental solutions of large temperature perturbation, the linear combination of the entropy mode encompasses the two dominating solutions and contributions originating from the vorticity modes. Hence, the fundamental solutions $m = 1, 2, 5, 6, 7, 8$ from Eqs. (84) and (85) in the form of interacting vorticity and entropy waves exist in this region. In other words, a total of four combinations exist: (1-3-5-6-7), (2-3-5-6-7), (1-3-5-6-8), and (2-3-5-6-8). To obtain a five-fundamental solution combination that isolates the entropy disturbance, the entropy mode must exhibit the least magnitude of vorticity. Both the vorticity and the temperature perturbation results are presented within the numerical result section. From the examination, although the temperature perturbation for all combinations has similar magnitudes, the combination (2-3-5-6-8) manifests the least vorticity in both the spanwise and streamwise directions. Hence, the entropy mode can be characterized by the following

$$\mathbf{z}_{\alpha\beta}^{EN} = c^{(2)}\mathbf{z}_{\alpha\beta}^{(2)} + c^{(3)}\mathbf{z}_{\alpha\beta}^{(3)} + c^{(5)}\mathbf{z}_{\alpha\beta}^{(5)} + c^{(6)}\mathbf{z}_{\alpha\beta}^{(6)} + c^{(8)}\mathbf{z}_{\alpha\beta}^{(8)}. \tag{35}$$

Similar to the acoustic and vorticity modes, the governing equation for each fundamental solution in the entropy mode can be expressed in the same way as Eq. (27) with $m = 2, 3, 5, 6, 8$ instead.

2.6. Bi-orthogonal eigenfunction system

Since the solution for Eq. (14) is not self-adjoint, a bi-orthogonal eigenfunction system can be introduced with an adjoint system. The adjoint solution acts as a filter for the direct solution and forms an orthogonality relationship between normal modes. We can introduce the general adjoint operator $\mathcal{L}^*$ from the inner product of a general vector $\mathcal{L}\mathcal{A}$ and $\mathcal{B}$.

$$\langle \mathcal{L}\mathcal{A}, \mathcal{B} \rangle = \langle \mathcal{A}, \mathcal{L}^*\mathcal{B} \rangle. \tag{36}$$

Let the operator $\mathcal{L}$ be the linear operator of Eq. (14) and $\mathcal{A} = \mathbf{A}_{\alpha\beta}$, we can introduce the following adjoint system with $\mathbf{B}_{\alpha\beta} = \mathcal{B}^*$, where the $*$ denotes the complex conjugate,

$$\frac{\partial}{\partial y}\left(\mathbf{L}_0^T \frac{\partial \mathbf{B}_{\alpha\beta}}{\partial y}\right) - \mathbf{L}_1^T \frac{\partial \mathbf{B}_{\alpha\beta}}{\partial y} = \mathbf{H}_1^T \mathbf{B}_{\alpha\beta} + i\alpha \mathbf{H}_2^T \mathbf{B}_{\alpha\beta} + i\beta \mathbf{H}_3^T \mathbf{B}_{\alpha\beta}$$
$$y = 0 : \quad B_{\alpha\beta_k} = 0, \quad k = 2, 4, 6, 8 \tag{37}$$
$$y \to \infty : \quad \left|B_{\alpha\beta_k}\right| < \infty, \quad k = 1, \dots, 16.$$

Here, the transpose is the conventional transpose. Similarly, the adjoint system can also be recast in the following form,

$$-\frac{d\mathbf{Y}_{\alpha\beta}}{dy} = \mathbf{H}^T \mathbf{Y}_{\alpha\beta}.$$
$$y = 0 : \quad Y_{\alpha\beta_k} = 0, \quad k = 2, 4, 6, 8 \tag{38}$$
$$y \to \infty : \quad \left|Y_{\alpha\beta_k}\right| < \infty, \quad k = 1, \cdots, 8$$

The solution $\mathbf{Y}_{\alpha\beta}$ can also be expressed as a combination of fundamental solutions, $\mathbf{V}_1 \cdots \mathbf{V}_8$, with the freestream fundamental solution vectors, $\mathbf{V}_k^0$, $k = 1, \cdots, 8$. The freestream fundamental solutions for the adjoint problem can be found using the cofactor of the freestream fundamental solution vector matrix from the direct problem. The transformation between $\mathbf{B}_{\alpha\beta}$ and $\mathbf{Y}_{\alpha\beta}$ can be referred to Tumin [16]. With the dual systems, the orthogonality condition exists as

$$i\left(\alpha - \alpha'\right) \int_0^\infty \left(\mathbf{H}_2\mathbf{A}_{\alpha\beta}, \mathbf{B}_{\alpha'\beta}\right) dy = 0. \tag{39}$$

This orthogonality relation can be obtained by integration by part of the dot product between $\mathbf{B}_{\alpha'\beta}$ and Eq. (14). The above equation can be rewritten into this form,

$$\left\langle \mathbf{H}_2\mathbf{A}_{\alpha\beta}, \mathbf{B}_{\alpha'\beta}\right\rangle = \int_0^\infty \left(\left(\mathbf{H}_2\mathbf{A}_{\alpha\beta}\right), \mathbf{B}_{\alpha'\beta}\right) dy = \Gamma\Delta_{\alpha\alpha'}. \tag{40}$$

According to [6], for the discrete modes, the term $\Delta_{\alpha\alpha'}$ represents a Kronecker Delta, which equals to 1 if the eigenvalues of the two modes are the same. This is because the decaying behavior of the discrete modes and the integral should result in a constant Γ value depending on the normalization. For the continuous modes, the same term represents a Dirac Delta. One can also derive the following inner product relation between $\mathbf{A}_{\alpha\beta}$ and $\mathbf{z}_{\alpha\beta}$. This would be helpful in the numerical implementation [16],

$$\left\langle \mathbf{H_2}\mathbf{A}_{\alpha\beta}, \mathbf{B}_{\alpha\beta}\right\rangle = -\mathrm{i}\left\langle \frac{\partial \mathbf{H}}{\partial \alpha}\mathbf{z}_{\alpha\beta}, \mathbf{Y}_{\alpha\beta}\right\rangle. \tag{41}$$

Proven in [6], any perturbation can be written as a combination of discrete and continuous modes. For a decomposition of the computational data $\mathbf{A}_D$ with the discrete modes and the continuous modes, the perturbation can be expressed as follows. The components of $\mathbf{A}_D$ are the spectral components of the perturbation variables for a given frequency, f. Here the coefficients C_n correspond to the modal coefficient of the nth discrete mode and $\mathbf{A}_{\alpha\beta_n}(y)$ is the discrete mode eigenfunction. The coefficients C_m refer to the coefficients of the mth continuous mode and $\mathbf{A}_{\alpha\beta_m}(y)$ is the corresponding wave shape function.

$$\mathbf{A}_D(x, y, f) \approx \sum_n^P C_n\mathbf{A}_{\alpha\beta_n}(y)e^{i\alpha_n x} + \sum_m^Q \int_0^\infty C_m\mathbf{A}_{\alpha\beta_m}(y)e^{i\alpha_m(K)x}dK, \tag{42}$$

where $P = 2$ represents the first two emerging discrete modes originating from the fast and slow acoustic spectrum. Note that although higher-order discrete modes also exist, the synchronization of the first discrete modes F and S is primarily responsible for the rise of the second mode instability. A decomposition including the higher modes can be performed in further studies for a more comprehensive investigation. And $Q = 5$ represents the number of continuous modes (fast and slow acoustic modes, two vorticity modes, and one entropy mode). An arbitrary Mth modal coefficient, C_M, where $M = n$ for the nth discrete mode and $M = m$ for the mth continuous mode, is as follows

$$C_M = \frac{\left\langle \frac{\partial \mathbf{H}}{\partial \alpha}\mathbf{z}_D, \mathbf{Y}_{\alpha\beta_M}\right\rangle}{\left\langle \frac{\partial \mathbf{H}}{\partial \alpha}\mathbf{z}_{\alpha\beta_M}, \mathbf{Y}_{\alpha\beta_M}\right\rangle}. \tag{43}$$

With $\mathbf{z}_{\alpha\beta_M}$ being the direct eigenfunction of the nth discrete mode or the jth continuous mode from Eq. (42) and $\mathbf{Y}_{\alpha\beta_M}$ being the adjoint eigenfunction obtained from Eq. (38) for the corresponding discrete or continuous mode. In practice, the numerical coefficients can be obtained by numerical integration of the dot product from the wall to the freestream using a composite trapezoidal rule which will be discussed later.

3. Numerical method: very high-order finite difference scheme on non-uniform grid

3.1. General problem setup

To start the numerical implementation, a multi-domain non-uniform grid distribution is defined to extract features in specific regions. Fig. 3 shows a schematic of the grid for the wall-normal profile,

Three domains are generally focused on extracting physical features in the hypersonic boundary layer flow. In hypersonic boundary layer flow, two high-gradient regions exist away from the wall, with one being the temperature gradient and one being the velocity gradient. Thus the first domain emphasizes the region between the wall and the critical layer where the maximum temperature gradient is located. The second domain ends when the streamwise velocity equals 95 percent of the freestream velocity. The third domain covers the rest of the profile. For each zone, the distribution of N number of grid points over the zone domain $[a, b]$ will follow Kosloff [43], Zhong [22], and Shukla [23],

$$y_i = \frac{b + a}{2} + (b - a)\frac{\sin^{-1}(-\alpha\cos(\pi i/N))}{2\sin^{-1}\alpha}, \quad i = 0, \cdots, N, \tag{44}$$

where the index i is shown in Fig. 3. The parameter α can be tuned to stretch the grid from a uniform grid ($\alpha = 1$), which introduces oscillation errors for higher order finite difference, to a Chebyshev grid ($\alpha = 0$). This stretching is tuned such that the discrete operator is stable while maintaining accuracy and efficiency. A typical value of the grid parameter α used in this chapter is 0.99 which is close near uniform except for the boundaries. Various trends of stable α tuning can be found in Zhong's work [22]. As the order of the scheme increases, the parameter α should increase in general. With this multi-domain non-uniform grid, the finite difference method
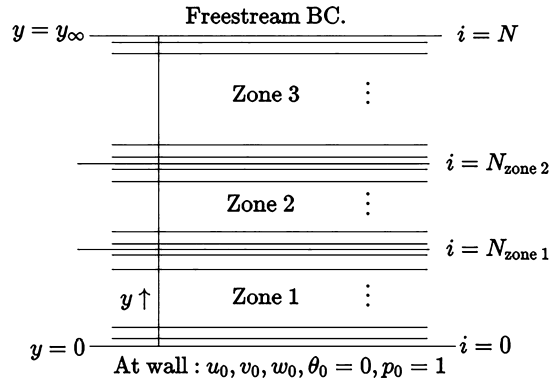
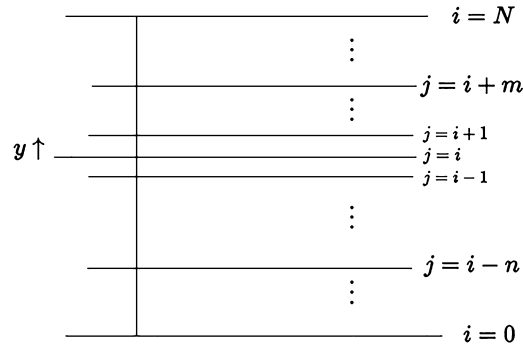**Fig. 3.** Schematic for a multi-domain grid distribution for the wall-normal profile.

Fig. 4. Schematic for finite difference stencil index over the grid index.

can achieve high-order accuracy while maintaining stability. Furthermore, this direct application of the finite difference method on a non-uniform grid eliminates the grid transformation procedure needed in the previous spectral collocation method by [17].

With the grid defined, we apply the finite difference method. In order to approximate the solution at each y_i, the local stencil of l points,

$$l = n + m + 1 \tag{45}$$

where n being the number of points before point i and m being the number of points after i, can be used. Under this convention, the stencil length l is used to identify the schemes in the future. Based on this grid, the differential equations of Eq. (15) can be solved with a finite difference method using the Lagrange polynomial. Here, the Lagrange polynomial can be applied to the vector $\mathbf{z}_{\alpha\beta}$ directly to approximate the ith point value,

$$\mathbf{z}_{\alpha\beta}(y_i) = \sum_{j=i-n}^{i+m} \mathbf{z}_{\alpha\beta}\left(y_j\right) l_j(y_i) \tag{46}$$

where the index i represents each point shown in Fig. 4. Note that this polynomial can be applied across the multi-domain without a domain boundary condition, which is needed for Chebyshev collocation [17]. The Lagrange coefficients can be computed as

$$l_j(y_i) = \prod_{k \neq j} \frac{y_i - y_k}{y_j - y_k} \tag{47}$$

By taking the derivative of the Lagrange polynomial over x, the first derivative for all points $i = 0, \cdots, N$ can be approximated as

$$\frac{d\mathbf{z}_{\alpha\beta}\left(y_i\right)}{d y_i} = \sum_{j=i-n}^{i+m} \mathbf{z}_{\alpha\beta}\left(y_j\right) a_{ji}, \quad i = 0, \ldots, N. \tag{48}$$

where the coefficient a_{ji} corresponds to the jth coefficient in the first derivative of the Lagrange polynomial for the point y_i, given as

$$a_{ji} = \sum_{p \neq j} \frac{1}{y_j - y_p} \prod_{q \neq (j,p)} \frac{y_i - y_q}{y_j - y_q} \tag{49}$$

Fig. 4 shows a schematic of the grid indexing for the finite difference method for a clearer representation of the indices.

where the index j refers to the jth point of the stencil over the discrete grid from Eq. (48). Note that for interior points, a symmetric stencil where $n = m$ is generally used. However, n and m will be different near the boundaries to formulate a one-sided difference, with the extreme cases of $n = 0$ at the wall or $m = 0$ at the freestream. To maintain the order of accuracy on the boundaries, $l + 1$ points will be used for the one-sided difference stencils. With the first derivative approximated at each y_i, the 8 by 8 matrix $\mathbf{H}$ of Eq. (15) also varies for each y_i location from $i = 0$ to N. Hence, the approximated Eq. (15) can be written as

$$\frac{d\mathbf{z}_{\alpha\beta}(y_i)}{dy_i} = \sum_{j=i-n}^{i+m} \mathbf{z}_{\alpha\beta}(y_j) a_{ji} = \mathbf{H}_i \mathbf{z}_{\alpha\beta}(y_i), \quad i = 0, \cdots, N. \tag{50}$$

Arranging terms, a homogeneous discrete system can be formulated with the interior points from $i = 1$ to $N - 1$ being

$$\sum_{j=i-n}^{i+m} \mathbf{A}_{ji} \mathbf{z}_{\alpha\beta}(y_j) = 0, \quad i = 1, \ldots, N - 1$$
$$\mathbf{A}_{ji} = a_{ji}\mathbf{I} - \mathbf{H}_i, \quad i = j \tag{51}$$
$$\mathbf{A}_{ji} = a_{ji}\mathbf{I}, \quad i \neq j.$$

where $\mathbf{I}$ is the 8 by 8 identity matrix. Note that near the boundary, the finite difference stencil will be asymmetric, $n \neq m$. An additional point, a total of $l + 1$ points, can be used to form the asymmetric stencils. With the numerical system of interior points defined, the specific boundary treatments of both discrete and continuous modes will contain both physical and numerical boundary conditions, which will be discussed later.

Furthermore, the discrete adjoint operators can be obtained in the same way. Following Eqs. (38) and (51), the discrete adjoint formula can be written as

$$\sum_{j=i-n}^{i+m} \mathbf{A}_{ji} \mathbf{Y}_{\alpha\beta}(y_j) = 0, \quad i = 1, \ldots, N - 1$$
$$\mathbf{A}_{ji} = -a_{ji}\mathbf{I} - \mathbf{H}^{\mathbf{T}}_i, \quad i = j \tag{52}$$
$$\mathbf{A}_{ji} = -a_{ji}\mathbf{I}, \quad i \neq j.$$

for the interior points of the adjoint problem. Similarly, a combination of physical and numerical boundary conditions for the different modes will be discussed later.

3.2. Boundary conditions for the boundary value problem approach

With the general system of the interior points derived above, the boundary equations for $i = 0$ and $i = N$ have to be determined in order to complete the system. For the boundary treatments, the discrete and continuous modes have different treatments for their boundary conditions both at the wall and freestream. These boundary conditions will include both physical conditions from Eq. (14) and numerical conditions such as one-sided difference. Hence, a generic one-sided difference scheme derived from the same method is implemented on both ends for now and the mode-specific physical boundary conditions will be discussed in the next sections. For the wall boundary block row, the one-sided difference with a stencil length of $l + 1$ points gives

$$\frac{d\mathbf{z}_{\alpha\beta}(y_0)}{dy_0} = \sum_{j=0}^{l+1} \mathbf{z}_{\alpha\beta}(y_j) a_{j0}. \tag{53}$$

As mentioned above, the wall stencil has $n = 0$ points below the $y = 0$ point and $m = l - 1$ points above the $y = 0$ point. Hence, including the $y = 0$ point, the wall stencil will also have l points. Since a one-sided difference is implemented for the boundaries. Similarly for the freestream boundary block row,

$$\frac{d\mathbf{z}_{\alpha\beta}(y_N)}{dy_N} = \sum_{j=N-(l+1)}^{N} \mathbf{z}_{\alpha\beta}(y_j) a_{jN}. \tag{54}$$

The above formulations complete the generic numerical one-sided difference boundary condition used in obtaining both discrete and continuous modes. Yet, the numerical boundary conditions are not sufficient to satisfy the physics of the modes. Although having the same wall boundary conditions, the discrete modes decay in the freestream while the continuous modes are neutral waves continuing into the freestream. Hence, the implementation of both physical conditions and numerical boundary conditions for both discrete and continuous modes will be discussed next.

3.2.1. Discrete mode boundary conditions

For the discrete modes, both physical conditions from Eq. (14) and numerical boundary conditions of Eqs. (53) and (54) will be applied. In this section, the wall and the freestream boundary conditions for the discrete mode will be presented. The one-sided difference of Eq. (53) can be applied to Eq. (51) to obtain a system at the $i = 0$ point,

$$\sum_{j=0}^{l+1} \mathbf{A}_{j0} \mathbf{z}_{\alpha\beta} \left(y_j \right) = 0$$
$$\mathbf{A}_{j0} = a_{j0}\mathbf{I} - \mathbf{H}_0, \quad j = 0$$
$$\mathbf{A}_{j0} = a_{j0}\mathbf{I}, \quad j \neq 0,$$

(55)

where $\mathbf{H_0}$ is the coefficient matrix $\mathbf{H}$ evaluated at $i = 0$. For the global eigenvalue decomposition, rows 1, 3, 5, and 7 of the above system can be replaced with the physical wall boundary conditions of Eq. (59). The complete system at the $i = 0$ point can be written as,

$$y = y_0: \quad \left(\sum_{j=0}^{l+1} \mathbf{A}_{j0} \mathbf{z}_{\alpha\beta} \left(y_j \right) \right)_k = 0, \quad k = 2, 5, 6, 8$$
$$\left(z_{\alpha\beta} \left(y_0 \right) \right)_k = 0, \quad k = 1, 3, 5, 7$$

(56)

where the $k = 2, 4, 6, 8$ rows are one-sided numerical boundary conditions from Eq. (55) and $k = 1, 3, 5, 7$ rows are replaced with the physical boundary conditions. Again, these boundary conditions are implemented directly in the system and the solution would yield the eigenpairs of the discrete modes directly. For the freestream boundary conditions at $i = N$, the decaying boundary conditions are enforced and can be written in an equation for the $i = N$ points,

$$y = y_N: \quad \mathbf{z}_{\alpha\beta} \left(y_N \right) = 0.$$

(57)

Combining these two boundary conditions with Eq. (51), the discrete system of all points $i = 0, \cdots, N$ forms a non-linear eigenvalue problem with respect to α. If the nonlinear terms with respect to α are omitted or α^2 is set to 0, a global $8N$ by $8N$ eigenvalue problem can be constructed as presented in Malik's work [17].

$$\sum_{j=i-n}^{i+m} \left(\mathbf{B}_{ji} - \alpha \mathbf{C}_{ji} \right) \mathbf{z}_{\alpha\beta} \left(y_j \right) = 0, \quad i = 0, \cdots, N$$
$$\text{where} \quad \left(\mathbf{B}_{ji} - \alpha \mathbf{C}_{ji} \right) = \mathbf{A}_{ji}.$$

(58)

with $\mathbf{B}_{ji}$ being a matrix of coefficients with no dependence on α and $\mathbf{C}_{ji}$ being otherwise. The global eigenvalue decomposition gives an approximation of the distribution of the discrete α.

To refine the value of the discrete mode eigenvalue and eigenfunctions by including the α^2 terms, a local non-homogeneous boundary value problem can be formulated by replacing $\theta(y_0) = 0$ with the wall pressure normalization, $p(y_0) = 1$. Hence, the wall boundary conditions for the local problem are

$$y = y_0: \quad \left(\sum_{j=0}^{l+1} \mathbf{A}_{j0} \mathbf{z}_{\alpha\beta} \left(y_j \right) \right)_k = 0, \quad k = 2, 5, 6, 8$$
$$\left(z_{\alpha\beta} \left(y_0 \right) \right)_4 = 1$$
$$\left(z_{\alpha\beta} \left(y_0 \right) \right)_k = 0, \quad k = 1, 3, 7$$

(59)

Note that since $(z_{\alpha\beta})_5 = \theta = 0$ is not enforced, the fifth row is the one-sided difference condition same as the 2, 6, 8 rows, with the above numerical and physical conditions, an equation at $i = 0$ can be expressed similarly as

$$y = y_0: \quad \sum_{j=0}^{l+1} \mathbf{A}_{j0} \mathbf{z}_{\alpha\beta} \left(y_j \right) = \mathbf{b}$$
$$(\mathbf{b})_k = 0, \quad k \neq 4$$
$$(\mathbf{b})_4 = 1,$$

(60)

The freestream boundary conditions will be the same as the global problem in Eq. (57). With these boundary conditions, a local non-homogeneous boundary value problem can be constructed with Eq. (51) and gives a solution with an eigenvalue α that does not satisfy $\theta(y_0) = 0$. Since the wall temperature is a function of the α, a nonlinear root-finding problem can be formulated to satisfy the temperature condition,

$$\theta(y_0) = f(\alpha) = 0$$

(61)

Since the discrete system combining Eqs. (51) and (59) has a nonlinear dependence on α, Newton's method is applied as a nonlinear search for the correct α that meets the temperature boundary condition. With a guessed value of α_0, the finite difference method is implemented to solve for the temperature or velocity fluctuation at the wall. For the temperature fluctuation, $\theta_{\text{wall}} = z_{\alpha_0 \beta_5}(0)$. at $y = 0$, the derivative of the discrete system at the wall is taken in the following equation with boundary conditions

$$y = y_0: \quad \sum_{j=0}^{l+1} \mathbf{A}_{ji} \frac{\partial \mathbf{z}_{\alpha\beta}(y_j)}{\partial \alpha} = \frac{\partial \mathbf{H}}{\partial \alpha} \mathbf{z}_{\alpha\beta}(y_0) + B.C. \tag{62}$$

where the boundary condition, $B.C.$, does not change with α for the discrete mode case. Note that the finite difference stencil coefficients A_{ji} do not depend on α either. By solving this equation, the gradient of the wall temperature $\frac{\partial \theta_0}{\partial \alpha}$ can be obtained by applying the Newton's iteration,

$$\alpha_{new} = \alpha_0 - \theta_0^{\alpha_0} \left(\frac{\partial \theta_0}{\partial \alpha} \right)^{-1}, \tag{63}$$

to get the new spatial eigenvalue. To solve for the linear system, the non-zero elements of the system are first stored as sparse matrices using the built-in *MATLAB* function *sparse*. Algorithms such as the sparse LU decomposition from *MATLAB* can be used to solve the linear system in Eq. (51) where the same LU decomposition can be used in Newton's iteration. Malik [17] also suggested keeping the same LU factorization for a small number of iterations before updating to further save computational cost.

For the adjoint solutions, since the same streamwise wavenumber α is shared between the direct and adjoint solutions, the iteration for α is not necessary. Thus, the four physical wall boundary conditions and one normalizing condition at $i = 0$,

$$y = y_0: \quad \left(Y_{\alpha\beta} \left(y_0 \right) \right)_k = 0, \quad k = 2, 4, 6, 8$$
$$\left(Y_{\alpha\beta} \left(y_0 \right) \right)_3 = 1, \tag{64}$$

can be applied directly. Here, the normalization of $(\mathbf{Y}_{\alpha\beta})_3 = 1$ is used. Combining with the numerical one-sided difference condition the equation at $i = 0$ can be expressed similarly to the direct problem.

$$y = y_0: \quad \sum_{j=0}^{l+1} \mathbf{A}_{j0} \mathbf{Y}_{\alpha\beta} \left(y_j \right) = \mathbf{b}$$
$$(\mathbf{b})_k = 0, \quad k \neq 3$$
$$(\mathbf{b})_3 = 1. \tag{65}$$

For the freestream conditions at $i = N$, the decaying condition of

$$y = y_N: \quad \left(Y_{\alpha\beta} \left(y_N \right) \right)_k = 0, \quad k = 1, \cdots, 8 \tag{66}$$

is enforced. This decaying condition can be expressed as the $i = N$ equation similar to Eq. (57). Combining the above boundary conditions with Eq. (52), a full system of $i = 0, \cdots, N$ is formulated and the adjoint solutions of the discrete modes can be obtained by solving such system.

3.2.2. Continuous mode boundary conditions

To enforce the boundedness behavior of the wall-normal direction exponential, $\exp(\lambda_m y_\infty) < \infty$, two types of solutions were introduced by Salwen and Grosch [6]. The first type is the discrete solution which decays in the freestream. The second is the continuous spectra which contain both neutral and decaying fundamental solutions in the freestream. These neutral asymptotic solutions known as continuous modes naturally form boundary value problems with forcing in the freestream. To obtain the bounded solutions, the mth wall-normal direction eigenvalue λ_m is set to have a neutral asymptotic behavior,

$$Re(\lambda_m) = 0, \quad m = 1, \cdots, 8 \tag{67}$$

by imposing Eq. (21) where K is real and positive. With a given frequency ω and spanwise wavenumber β, the streamwise wavenumber α can be solved directly from Eq. (83). Note that the $\lambda(\alpha)$ relation is non-linear and can be solved with Brent's method following Miselis [34].

With a determined α value, each continuous mode can be formulated as a linear combination of 5 or fewer fundamental solutions as discussed in the previous section. Thus, the discussion of numerical implementation will follow the conventional 5 fundamental solution combinations from Tumin [16] to be generic. An example of solving for the spanwise vorticity mode is presented in this section and other continuous modes should follow the same procedure. With the following combination by Tumin,

$$\mathbf{z}_{\alpha\beta}^{VA} = c^{(1)} \mathbf{z}_{\alpha\beta}^{(1)} + c^{(2)} \mathbf{z}_{\alpha\beta}^{(2)} + c^{(3)} \mathbf{z}_{\alpha\beta}^{(3)} + c^{(5)} \mathbf{z}_{\alpha\beta}^{(5)} + c^{(7)} \mathbf{z}_{\alpha\beta}^{(7)}, \tag{68}$$

the spanwise vorticity mode can be obtained with coefficients $c^{(m)}$ for the mth fundamental solution determined to satisfy the wall boundary conditions from Eq. (15) and the wall pressure normalization. Since five fundamental solutions are required to form a continuous mode, the finite difference method of Eq. (51) will be applied 5 times to obtain each mth fundamental solution. The asymptotic boundary conditions $\mathbf{z}_{\alpha\beta_0}^{(m)}$ presented in Eqs. (84) and (85) are applied as freestream boundary conditions,

$$y \to \infty: \mathbf{z}_{\alpha\beta}^{(m)} = \mathbf{z}_{\alpha\beta_0}^{(m)}, \quad m = 1, 2, 3, 5, 7. \tag{69}$$

This boundary condition can also be written in a numerical equation at $i = N$

$$y = y_N: \quad \mathbf{z}_{\alpha\beta}^{(\mathbf{m})}\left(y_N\right) = \mathbf{z}_{\alpha\beta_0}^{(\mathbf{m})}, \quad m = 1, 2, 3, 5, 7. \tag{70}$$

The wall boundary conditions will not be imposed when solving each fundamental solution. Instead, the physical boundary conditions at the wall will be satisfied by the unique set of coefficients. Thus, the one-sided difference of Eq. (53) is implemented for the $i = 0$ point for each mth fundamental solution,

$$y = y_0: \quad \sum_{j=0}^{l+1} \mathbf{A}_{j0}\mathbf{z}_{\alpha\beta}^{(\mathbf{m})}\left(y_j\right) = 0, \quad m = 1, 2, 3, 5, 7. \tag{71}$$

Combining the above equations, a discrete system of equations from $i = 0$ to N for each fundamental solution $\mathbf{z}_{\alpha\beta}^{(\mathbf{m})}$ can be obtained. Although for each continuous mode, five fundamental solutions have to be solved, the computational cost can still be low since the finite difference linear operator is banded and sparse. Furthermore, since the wavenumber α and other matrix coefficient parameters are shared between fundamental solutions in a particular mode, the same LU decomposition of the discrete operator can be used to solve for all fundamental solutions within a combination.

After obtaining each fundamental solution with the finite difference method, the fundamental solutions at the wall, $\mathbf{z}_{\alpha\beta}^{(\mathbf{m})}(y_0)$, do not satisfy the physical wall boundary conditions from Eq. (15) and the wall pressure normalization. Instead, Eq. (28) is solved to obtain the coefficients $c^{(m)}$ that can be used to superpose the fundamental solutions to satisfy the boundary conditions. After obtaining the coefficients, the superposition of a continuous mode can be performed,

$$\mathbf{z}_{\alpha\beta} = c^{(1)}\mathbf{z}_{\alpha\beta}^{(\mathbf{1})} + c^{(2)}\mathbf{z}_{\alpha\beta}^{(\mathbf{2})} + c^{(3)}\mathbf{z}_{\alpha\beta}^{(\mathbf{3})} + c^{(5)}\mathbf{z}_{\alpha\beta}^{(\mathbf{5})} + c^{(7)}\mathbf{z}_{\alpha\beta}^{(\mathbf{7})}. \tag{72}$$

A similar procedure can be applied to obtain the rest of the continuous modes with the only difference in the fundamental solution combination and the corresponding eigenvalue λ_m. In addition, since the freestream wavenumber α of the fast and slow acoustic modes are isolated from the other branches, shown in Fig. 2. These two acoustic modes can be obtained without using linear combinations. A linear system combining the wall conditions of Eq. (15) at $y = 0$, the interior points of Eq. (51) for $i = 1, \cdots, N-1$, and the one-sided difference extrapolation of Eq. (54) for $i = N$ can be used to solve for the two acoustic modes directly.

To describe the behavior of the whole continuous branch, the contribution from all branch wavenumber values K_l for $l = 1, \cdots, N$ should be summed as

$$\mathbf{A}_{\alpha\beta}(y) = \int_0^K C(K')\mathbf{A}_{\alpha(\mathbf{K}')\beta}(y)dK' \approx \sum_{l=1}^N C\left(K_l\right)\mathbf{A}_{\alpha(\mathbf{K_l})\beta}(y)\Delta K. \tag{73}$$

Furthermore, the adjoint freestream fundamental solutions are obtained mathematically by defining the adjoint of the direct freestream fundamental solution following the cofactor matrix following Tumin [16]. With the adjoint freestream fundamental solutions, the continuous mode adjoint solutions can also be solved in the same way as the direct continuous modes with the corresponding wall boundary conditions.

3.3. Bi-orthogonal decomposition

After formulating the numerical procedure to obtain both discrete and continuous modes, the bi-orthogonality relationship between the direct and adjoint eigenfunctions can be used as a filter to isolate the modal behavior. For the implementation, an inner product between the direct and adjoint eigenfunctions is used in Eqs. (40) and (41). From Eq. (41), we can write

$$\left\langle \frac{\partial\mathbf{H}}{\partial\alpha}\mathbf{z}_{\alpha\beta}, \mathbf{Y}_{\alpha\beta} \right\rangle = \int_0^\infty \left(\frac{\partial\mathbf{H}}{\partial\alpha}\mathbf{z}_{\alpha\beta}, \mathbf{Y}_{\alpha\beta}\right)dy = \Gamma\Delta_{\alpha\alpha'}. \tag{74}$$

Using a non-uniform trapezoidal rule, the integration can be numerically implemented as the following. Let f be the function of the dot product inside the integral for Eq. (74),

$$\int_0^\infty f\,dy \approx \sum_{K=1}^N \frac{f(y_{k-1}) + f(y_k)}{2}\Delta y_k, \tag{75}$$

where ∞ is approximated at the freestream upper bound y_{max} location of the domain. Hence, from the inner product of the direct and adjoint solutions of the same mode, the normalization value, Γ, can be calculated for both discrete and continuous modes. Note that the normalization is dependent on the normalization boundary conditions mentioned above. A consistent normalization across the modes is necessary. After obtaining Γ, Eq. (43) can be utilized to compute the amplitude of modal contribution for a perturbed flowfield. Again, the contribution amplitude of a particular mode in a perturbation is computed with an inner product of the perturbed flowfield and the corresponding mode's adjoint eigenfunctions with the normalization.

The adjoint wall boundary condition is applied similarly to the direct problem boundary condition except that the spatial wavenumber α is shared between the two systems and is converged by Newton's method in the direct problem. Hence, the four wall boundary conditions in Eq. (52) can be applied directly. The adjoint decaying freestream boundary condition also has decaying conditions and can be applied.
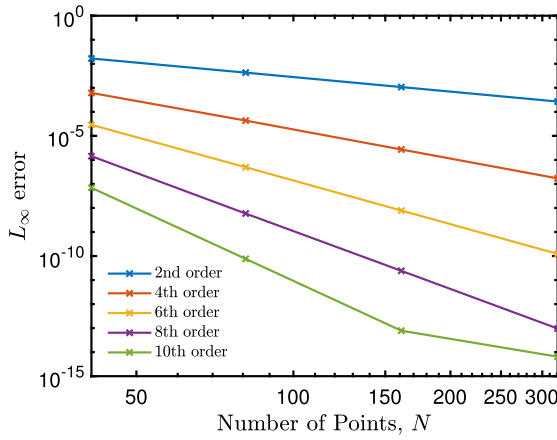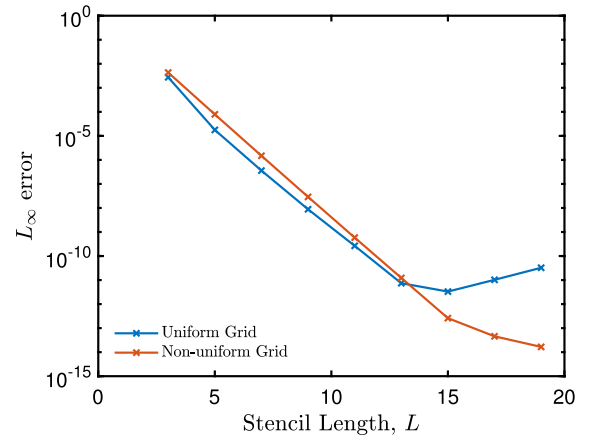
(a) L_∞ errors for the derivative to the Bessel function.   (b) L_∞ errors for various grid distributions.

Fig. 5. Order of accuracy verification for the high-order finite difference scheme over a non-uniform grid. (For interpretation of the colors in the figure(s), the reader is referred to the web version of this article.)

4. Results

4.1. Verification of finite difference scheme

To study the convergence behavior of the finite difference scheme, a test case using the Bessel function of the first kind is solved for its first derivative since the exact derivative can be obtained with the *MATLAB* built-in function. The finite difference scheme is used on the zeroth-order Bessel function values and the result is compared with the first-order Bessel function values. To verify the convergence, test trials are made of a range of different numbers of grid points and stencil lengths. Fig. 5 presents the error behaviors when the various finite difference schemes are applied to the Bessel function.

Fig. 5a is the infinity norm error versus the number of grid points for different stencils on the non-uniform grid. From Fig. 5a, We can see that the error decreases according to the predicted trends and reaches 10^{-14} to 10^{-15}. For the non-uniform grid, we set the number of grid points $N = 101$ and varied the lengths of stencils. The grid tuning parameter α is set to be 0.95 to satisfy the stability for the lengths of stencils used according to Zhong and Tatineni [22]. Fig. 5b is a comparison between the uniform and non-uniform grid errors. From Fig. 5b, the L_∞ error for the non-uniform grid reaches 10^{-14} for the stencil length of 17 in contrast to the error stagnating at 10^{-10} for the uniform grid, which is a stability issue for the uniform grid due to the Runge phenomena near the boundary points. Hence, the method presented in this paper deploys the non-uniform stretching grid, allowing high-order accuracy and stability to be maintained at the boundary.

4.2. Bi-orthogonal eigenfunction system of compressible flow over a flat plate

In this section, the goal is to confirm that the discrete and continuous eigenfunctions are computed accurately. These eigenpairs are critical in the bi-orthogonal decomposition and necessary tools for obtaining the modal effects of perturbations. Hence, a verification of eigenpairs both discrete and continuous modes against previous work is performed to ensure the correctness of the result. Since the compressible flow over a flat plate has been studied in depth [16] [17] [44], such case can be used as the verification of the new numerical method by comparing eigenpairs. For the compressible flow over a flat plate, the meanflow profile is obtained through a similarity transformation following Malik's conventions [17]. No slip velocity boundary condition is applied at the wall. The meanflow wall temperature boundary conditions can be varied between an adiabatic wall and an isothermal wall given the nature of the problem. The flat plate meanflow profile is solved by a shooting method using the fourth-order Runge-Kutta and Newton's method since the flat plate meanflow can be easily converged.
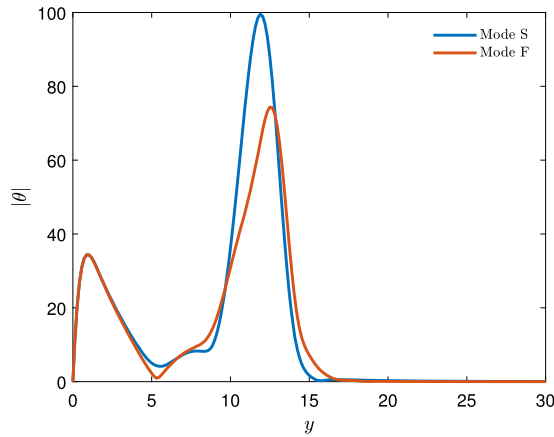
4.2.1. Discrete modes

As mentioned above, Balakumar and Malik [44] and Miselis [34] presented the result for a case of compressible flow over a flat plate with a Mach number of 4.5. The stagnation temperature is 311 K. Adiabatic wall meanflow is set. The Prandtl number is 0.72 and the Reynolds number is $Re = 1000$. The non-dimensional circular frequency ω is set to 0.2 and the non-dimensional spanwise wavenumber β is set to 0.12. The wall pressure is chosen as the normalization variable. The table below is the comparison of results for the case. The finite difference scheme is set to have a stencil length of 11 with the number of grid points $N = 204$. For this case, a single domain non-uniform grid is used. The grid stretching parameter, α_{grid} is set to be 0.99. This parameter is chosen to satisfy the stability trend presented in [22]. To obtain the initial guesses for the local nonlinear iteration, a global eigendecomposition is performed. Fig. 2 shows the global eigenvalues with discrete poles and the discretized continuous branches of this case. The local nonlinear iteration is then applied to obtain the exact values of the two discrete modes. Fig. 6a shows the magnitude of the
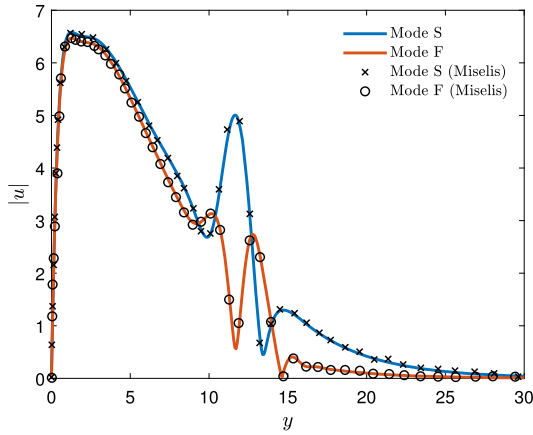
(a) Magnitude of streamwise velocity.
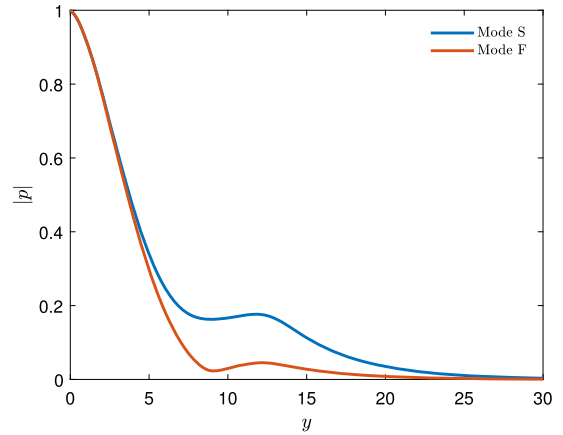
(b) Magnitude of pressure.

(c) Magnitude of temperature.

Fig. 6. Discrete Mode Results obtained with the direct solve method plotted against Miselis (2016).

Table 1
Spatial eigenvalue result comparison.

	Balakumar & Malik (1992)	Miselis (2016), Rk4, $N = 3000$	Finite Difference, $N = 204$
Mode S	$0.2181 + i2.969 \times 10^{-4}$	$0.2181 + i2.973 \times 10^{-4}$	$0.21813 + i2.9734 \times 10^{-4}$
Mode F	$0.2124 + i1.288 \times 10^{-2}$	$0.2124 + i1.288 \times 10^{-2}$	$0.21245 + i1.2886 \times 10^{-2}$

streamwise velocity component, $|u|$, plotted against the reference eigenfunction in [34]. Moreover, Figs. 6b and 6c show the pressure and temperature profiles of the discrete modes.

The eigenfunctions presented are normalized by the wall pressure. Overall behavior and the mode shape of the two discrete modes align well with the reference. The expected freestream decaying behavior is shown in all three perturbation variables. Two critical layers are present in the mode profiles. One corresponds to the peak in the temperature profile starting at the non-dimensional wall normal distance of $y = 10$ and the other corresponds to the peak in the streamwise velocity profile starting at the wall. In addition, the converged spatial eigenvalue α is compared in Table 1 with results from [44] and [34]. With only $N = 204$ grid points, the finite difference results show no discrepancy up to the given precision compared with results from [34]. Furthermore, with an 11-point stencil, the linear operator required is sparse in comparison to the spectral method. This computation can be as efficient as the initial value problem approach using the *MATLAB* sparse setting. The memory cost is also low as the sparse operator only stores the non-zero entries.

In addition, the multi-domain grid can be adjusted to focus on resolving features in the two peaking regions. From both the eigenvalues and eigenfunctions, we can conclude that the finite difference method is correctly implemented with consistency for the flat plate geometry.
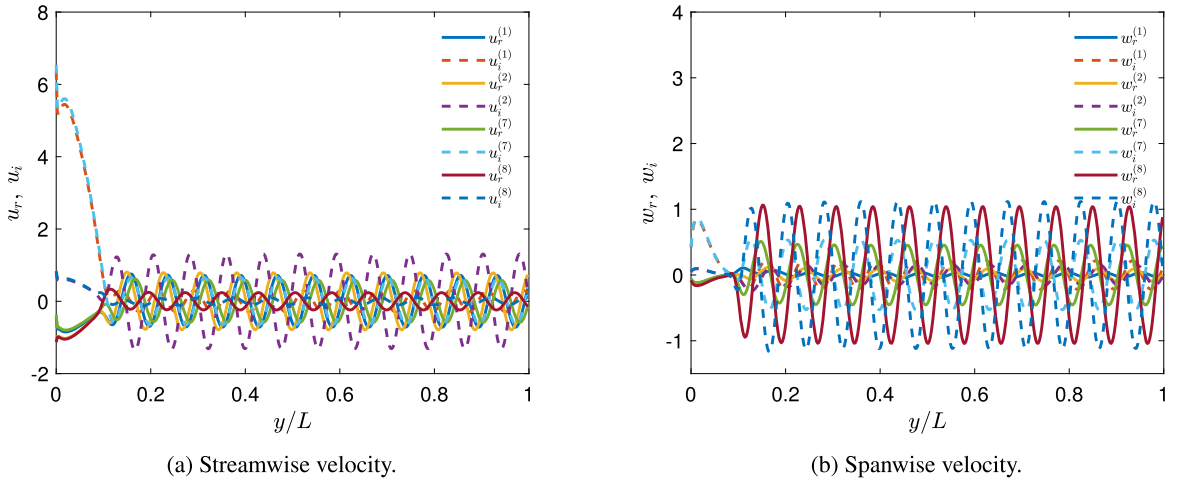
(a) Streamwise velocity.   (b) Spanwise velocity.

Fig. 7. The streamwise velocity (u_r, u_i) and spanwise velocity (w_r, w_i) plotted for the fundamental solutions, $m = 1, 2, 7, 8$ ($K = 1$).

4.2.2. Continuous modes

After verifying the discrete mode eigenvalues and eigenfunctions, the next goal is to verify the finite difference method with continuous modes. As mentioned in the section on governing equations, the continuous branches in the overlapping region include various non-decaying fundamental solutions. For example, the spanwise vorticity mode eigenvalues are identical to the streamwise vorticity mode eigenvalues from Eq. (83). Thus, for these two modes, both fundamental solution pairs of Eq. (84) are non-decaying. Combining the decaying and non-decaying fundamental solutions, two combinations exist for each vorticity mode. For example, the combinations (1-2-3-5-7) and (1-2-3-5-8) are the choices of the spanwise vorticity mode. While Tumin [16] verified the correct combination to be (1-2-3-5-7) via *Mathematica*, the intricate math procedure lacks a physical interpretation for each combination and its corresponding fundamental solutions. Thus, the first half of this section will present the fundamental solution results of different combinations to showcase the physical behavior of each fundamental solution and validate the combinations for the overlapping continuous modes.

Before the inspection of the fundamental solution combinations, each fundamental solution with asymptotic behavior of Eqs. (84) and (85) can be examined for their physical properties. A case of compressible flow over a flat plate with a Mach number of 5.95 following Tumin [16] and Miselis [34] is used to demonstrate the idea. The value of the branch parameter K is set to 1 in each case. The Prandtl number is set to 0.72 and the bulk viscosity is set to 0.8. Instead of adiabatic wall, the wall temperature to adiabatic wall ratio T_w/T_{ad} is set to 0.1 allowing heat transfer in the meanflow. The non-dimensional frequency F is set to 10^{-4}. The non-dimensional spanwise wave number β is 0.16 and the stagnation temperature is 640 K. The Reynolds number is 1500. The fundamental solutions are obtained with the boundary value problem approach by solving Eq. (51) with the boundary conditions of Eqs. (53) and (70). A 21-point finite difference stencil on a $N = 804$ grid is implemented for accuracy and clarity. Fig. 7 presents the streamwise velocity and the spanwise velocity of the fundamental solutions $m = 1, 2, 7, 8$, while Fig. 8 presents the pressure and temperature components of fundamental solutions $m = 3, 4, 5, 6$. Each fundamental solution is computed as a function of the meanflow variables and its corresponding eigenvalue from Eq. (83). From Figs. 7 and 8, it is evident that the perturbations associated with the fundamental solutions $m = 3, 4, 5, 6$ exhibit a higher overall magnitude, primarily due to their different normalization. Note that the overall normalization of the fundamental solutions is performed at a subsequent stage when the coefficients of each fundamental solution are computed with boundary conditions. Nevertheless, the relative comparison of the fundamental solution behavior can still be made. Upon examining the streamwise velocity perturbation in Fig. 7, it becomes apparent that the spanwise vorticity-dominated fundamental solutions $m = 1, 2$ exhibit higher perturbation magnitudes in u in contrast to the other vorticity-dominated mode $m = 7, 8$. Similarly, from the spanwise velocity comparison, the fundamental solutions $m = 7, 8$ have a greater perturbation than the fundamental solutions $m = 1, 2$. Furthermore, from the pressure perturbations shown in Fig. 8, the fundamental solutions $m = 5, 6$ reveal decaying pressure behaviors while $m = 3, 4$ display pressure oscillations. Additionally, the temperature perturbations of the fundamental solution $m = 5, 6$ shown indicate that the physical behavior of this particular pair of fundamental solutions is governed by entropy relations. Consequently, after the analysis of individual fundamental solutions, which provides insights into the dominant fundamental solutions within each continuous mode, it is feasible to investigate the combinations of fundamental solutions comprising each continuous mode.

To determine the appropriate set for the vorticity modes, the spanwise and streamwise vorticity components of each combination can be examined. In the following examples, the flow conditions are the same as the above fundamental solutions except that the Reynolds number is set to 2300. Fig. 9 shows a comparison of the streamwise and spanwise vorticity components between the two combinations. From the plot, the first combination, (1-2-3-5-7), contains less streamwise vorticity than the second combination, (1-2-3-5-8). Hence, the first combination aligns more with the definition of the spanwise vorticity mode. This can be confirmed again by the orthogonality check presented in the next section.
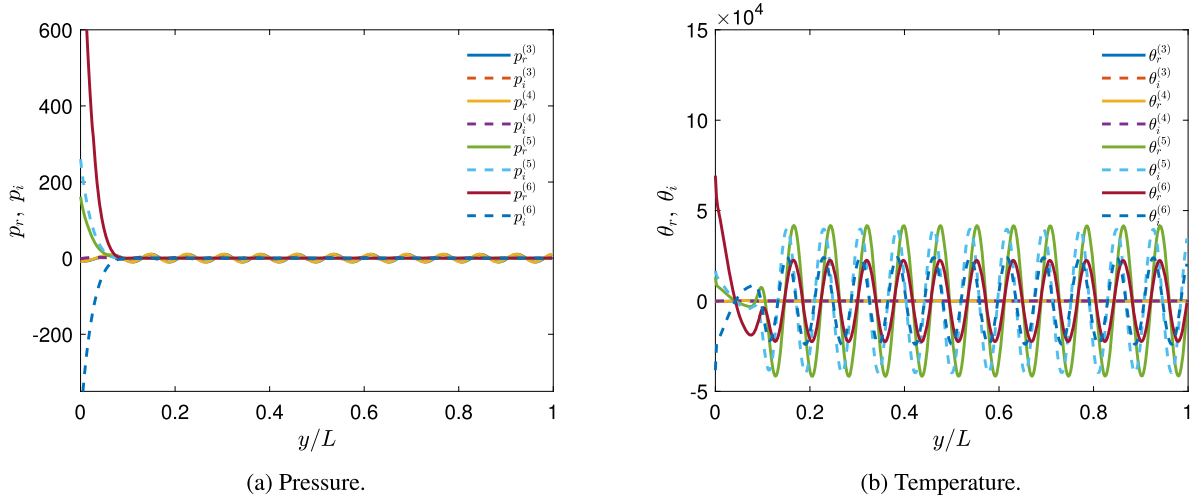
(a) Pressure.   (b) Temperature.

Fig. 8. The pressure perturbation (p_r, p_i) and temperature perturbation (θ_r, θ_i) plotted for the fundamental solutions, $m = 3, 4, 5, 6$ ($K = 1$).
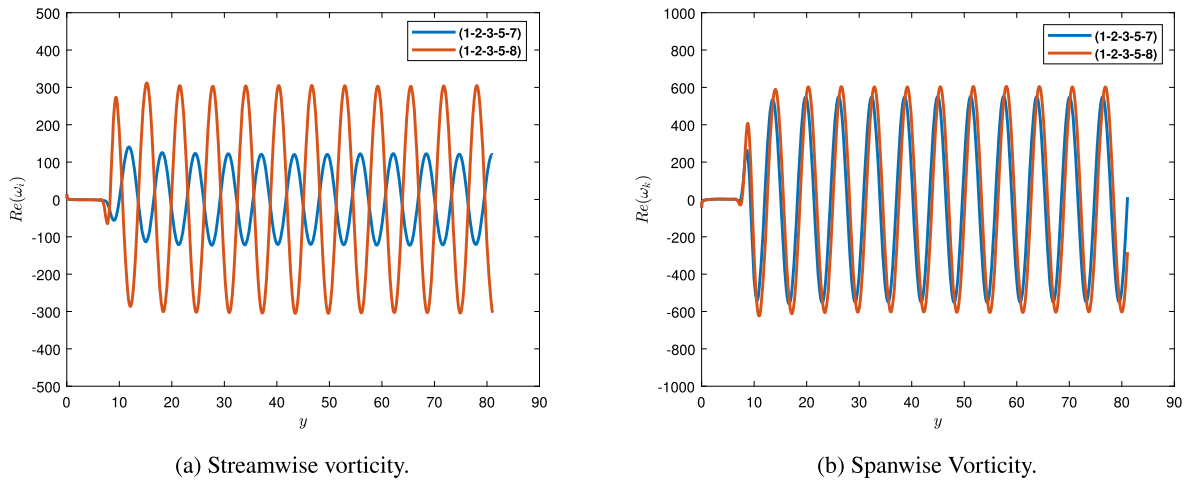

(a) Streamwise vorticity.   (b) Spanwise Vorticity.

Fig. 9. Comparison of vorticity components between two combinations of the spanwise vorticity mode ($M_\infty = 5.95$, $Re = 2300$, $\omega = 0.23$, $K = 1$).

The streamwise vorticity mode can also be determined similarly. For the entropy mode, in addition to the two pairs of non-decaying fundamental solutions by the vorticity modes, an extra pair of fundamental solutions $m = 5, 6$ is non-decaying in the vicinity of the branch point. Thus, both the vorticity and temperature perturbations should be examined to obtain the correct combination. Fig. 10 shows a comparison of the streamwise and spanwise vorticity components as well as the temperature perturbations between the four combinations. From the results, all four combinations have similar magnitudes for the temperature perturbation while the combination (2-3-5-6-8) results in the least spanwise and streamwise vorticity. So far, the physical results of different fundamental solution combinations are presented and each combination presented by Tumin [16] best aligns with the expected physical behavior. Further verification is performed using the bi-orthogonal relationship to ensure the bi-orthogonality between the modes in a later section. After verifying the correctness of the combinations, the next step in the verification would be comparing each continuous mode computed by the new numerical method.

For the continuous modes, the asymptotic boundary condition for vorticity and entropy modes as well as the one-sided extrapolation for acoustic modes are both implemented for demonstration. Figs. 11a and 11b show the streamwise velocity eigenfunctions, plotted against the results given by Tumin [16], for the two continuous acoustic modes obtained using the one-sided extrapolation. A grid convergence presented later demonstrates the convergence of modes at a grid of 204 points. The eigenfunctions presented here are normalized by the derivative of streamwise velocity at the wall, du/dy, rather than the wall pressure following Tumin's convention. Here, the non-dimensional wall normal coordinate, y, is normalized by the length of the wall-normal profile, L. The grid stretching parameter, α_{grid} is set to be 0.95 and the length of the stencil is also 21. In Figs. 11a and 11b, a grid convergence test is performed. The results show convergence at as least as $N = 104$ and the results align accurately for $N = 204$. From this grid convergence test, the number of grid points required to obtain the correct eigenfunctions is less than the initial value approach by Tumin [16] which needs a minimum of 601 points.
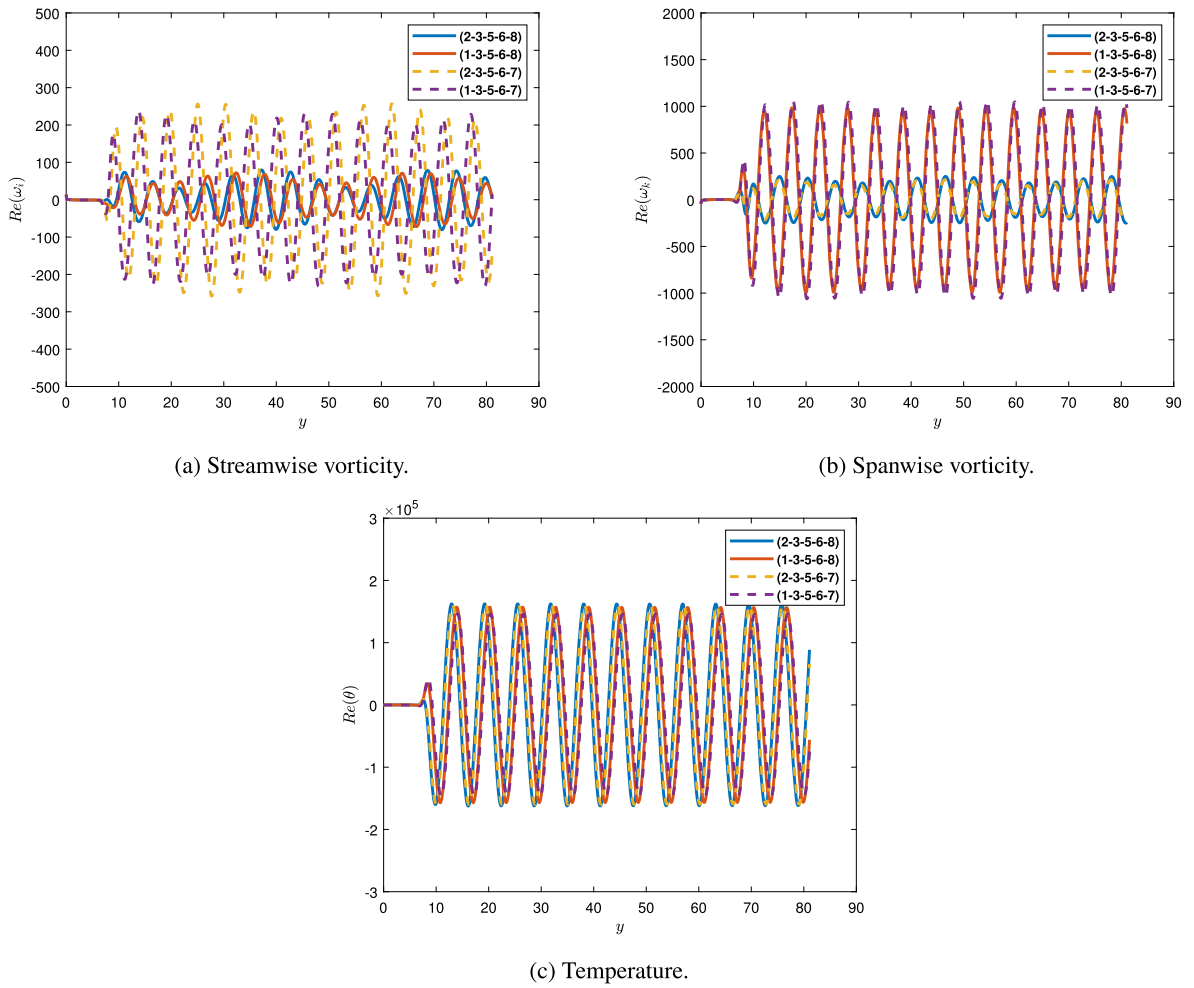
(a) Streamwise vorticity.

(b) Spanwise vorticity.

(c) Temperature.

Fig. 10. Comparison of vorticity and temperature components between four combinations of the entropy mode ($M_\infty = 5.95$, $Re = 2300$, $\omega = 0.23$, $K = 1$).
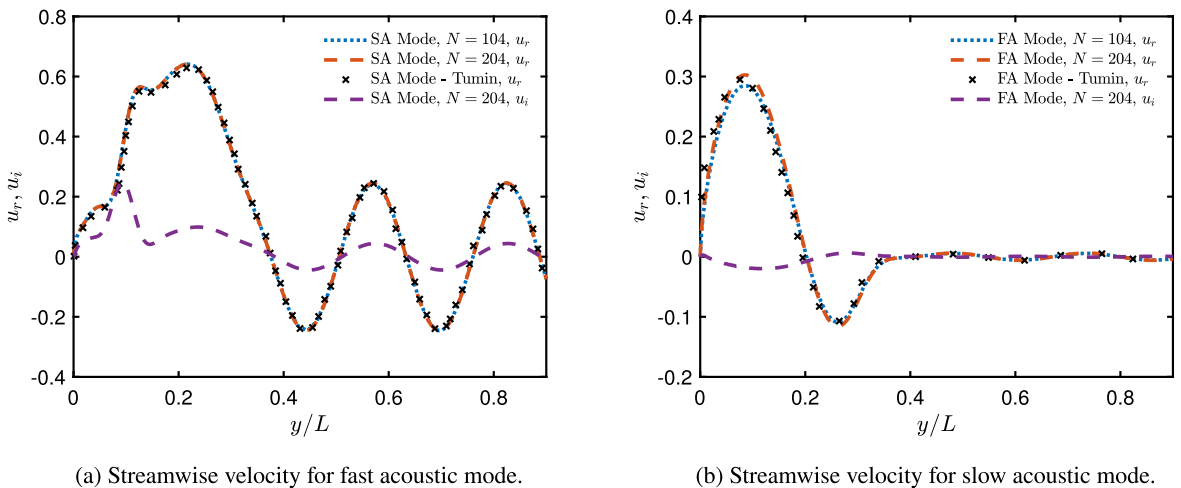

(a) Streamwise velocity for fast acoustic mode.

(b) Streamwise velocity for slow acoustic mode.

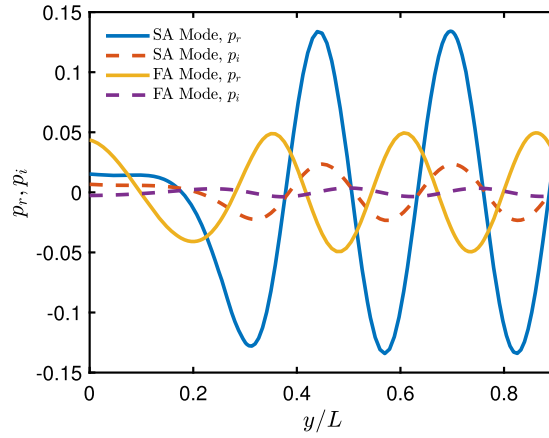**Fig. 11.** The computed continuous slow and fast acoustic mode eigenfunctions of streamwise velocity, compared with Tumin (2007).

Fig. 12. Pressure for slow and fast acoustic modes, $N = 201$.

The pressure components of the fast and slow acoustic modes are also shown in Fig. 12 for analysis of the pressure perturbations. Both the real and imaginary components of the eigenfunctions are plotted to showcase the behavior. From Fig. 12, the fast acoustic mode has a higher perturbation inside the boundary layer which has its edge near $y/L = 0.2$.

From the results shown in Fig. 11, the acoustic modes have a larger velocity perturbation amplitude inside the boundary layer and small oscillations continuing into the freestream. This behavior is different in the entropy and vorticity modes, which are presented in the following. For entropy and vorticity modes, the asymptotic boundary condition is implemented through the boundary value approach. Although the asymptotic boundary condition implementation requires solving Eq. (32) five times, the computation can still be cost-effective as the same LU decomposition can be applied. Fig. 13 shows the entropy and vorticity A continuous mode eigenfunctions. The streamwise velocities shown in Figs. 13a and 13b are compared with [16]. The wall-normal velocity and temperature eigenfunctions are also plotted for the vorticity and entropy modes in Figs. 13c and 13d. To have a more accurate comparison, the modes in Fig. 13 are resolved with $N = 404$ points. From the comparison, the eigenfunctions behave as expected. The small discrepancies in a few areas are due to the plot digitization. From the streamwise velocity eigenfunctions, both the entropy and vorticity modes have amplitudes that are higher in the freestream region and do not penetrate into the boundary layer. Moreover, the vorticity mode has a higher wall-normal velocity amplitude in comparison to the entropy mode, which agrees with the physical interpretation of the modes. Likewise, the temperature fluctuation is much higher in the entropy mode.

With the above comparisons between the computed results and existing results, the new finite difference method is verified to compute both discrete and continuous modes accurately.

4.2.3. Bi-orthogonal decomposition

With both the discrete modes and the continuous spectrum verified for different cases, the verification of the bi-orthogonal relationship will proceed. In this process, a case with flow conditions the same as the continuous spectrum verification case, but with a different Reynolds number of 2300, is presented. The grid parameters are also the same as the continuous spectrum case. The discrete mode eigenfunctions of this case are shown in Fig. 14a and the continuous acoustic modes are shown in Fig. 14b.

Since the decomposition purpose is to decompose an arbitrary disturbance and determine the amplitude of influence for each mode. The verification process begins with a composition of direct discrete and continuous modes, carrying different assigned coefficients, to form an arbitrary disturbance. Then the bi-orthogonal decomposition is deployed to decompose the designed disturbance in an attempt to recover the assigned coefficients for each mode. In this example, the discrete modes S and F as well as the fast and slow acoustic continuous modes are combined to form the arbitrary disturbance, $\mathbf{A}_D$.

$$\mathbf{A}_D = C_S \mathbf{A}_S + C_F \mathbf{A}_F + C_{SA} \mathbf{A}_{SA} + C_{FA} \mathbf{A}_{FA}, \tag{76}$$

Fig. 15 presents different reconstructed arbitrary signals using the discrete modes and the acoustic modes compared to Tumin [16]. Two cases are shown in Fig. 15 with the first one being a combination of discrete modes and fast acoustic mode only and the second being discrete modes and slow acoustic mode. The design coefficients C used in Fig. 15a are $C_S = 1$, $C_F = -1$ and $C_{FA} = 2$ and the coefficients used in Fig. 15b are $C_S = 1$, $C_F = -1$ and $C_{SA} = 2$.

Applying the orthogonality relation, the decomposition of this signal recovers the weights of $C_S = 1.0405 - 4.5385 \times 10^{-3} i$, $C_F = -9.9667 \times 10^{-1} + 2.6732 \times 10^{-2} i$ and $C_{FA} = 1.9999 + 1.2374 \times 10^{-5} i$. The relative error is around 4 percent to the assigned weights. Furthermore, the recovered coefficients are $C_S = 1.0186 - 2.7147 \times 10^{-3} i$, $C_F = -1.0155 + 3.8610 \times 10^{-4} i$ and $C_{SA} = 2.0000 - 2.1073 \times 10^{-7} i$ with the largest relative error around 2 percent to the assigned coefficients. From the examples above, the very high-order finite difference method to construct the bi-orthogonal eigenfunction system has been verified for the case of compressible flow over a flat plate.
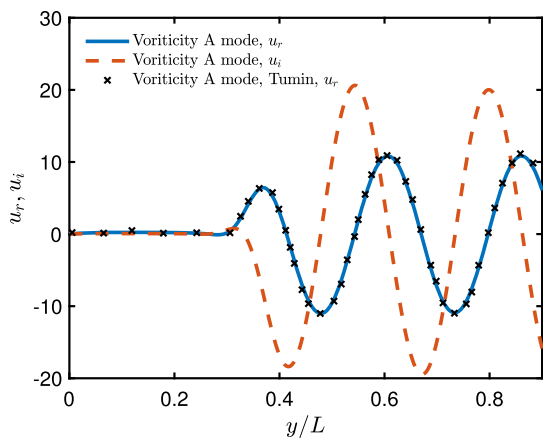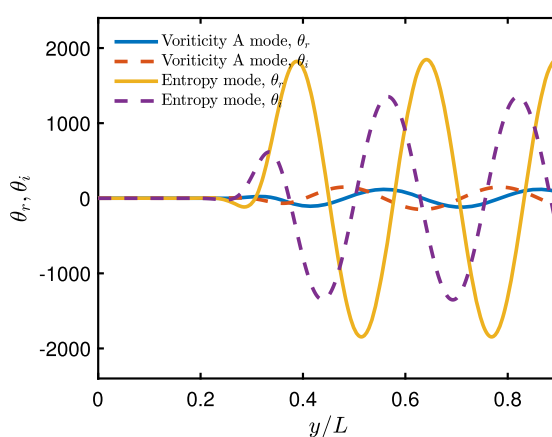
(a) Streamwise velocity for VA mode.
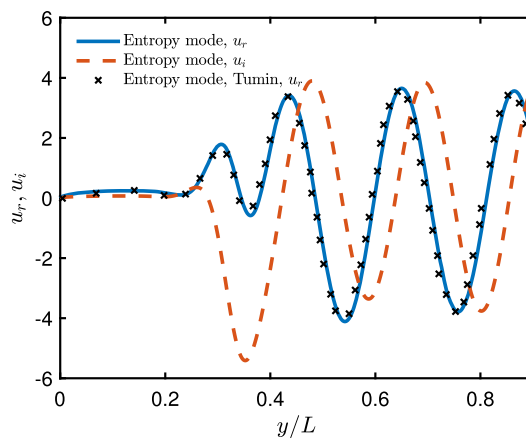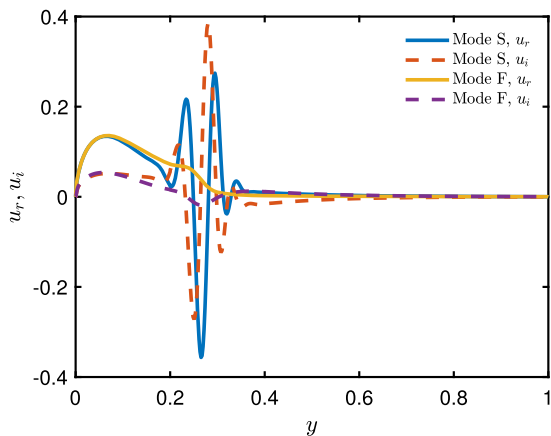

(b) Streamwise velocity for entropy mode.
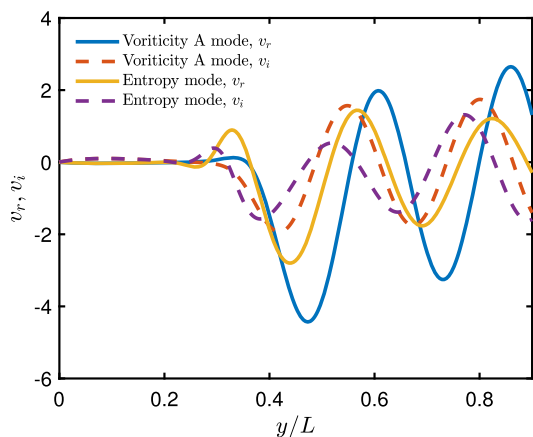
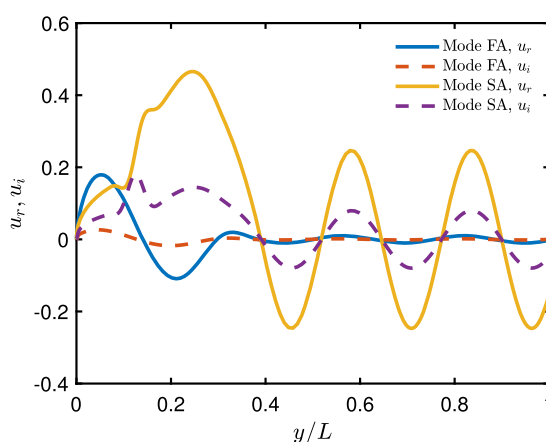(c) Wall normal velocity for vorticity A and entropy mode.

(d) Temperature for vorticity A and entropy mode.

Fig. 13. The computed continuous vorticity A and the entropy mode eigenfunctions of streamwise velocity, compared with Tumin (2007), wall-normal velocity, and temperature.
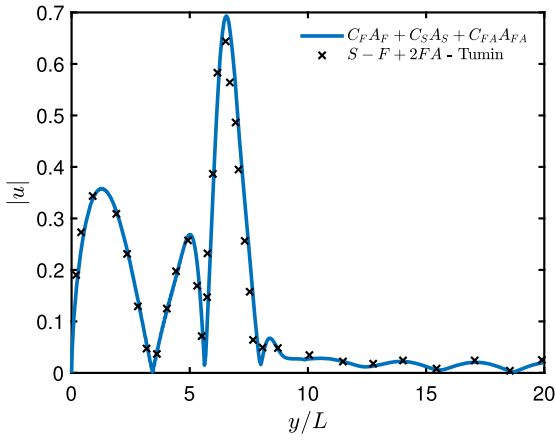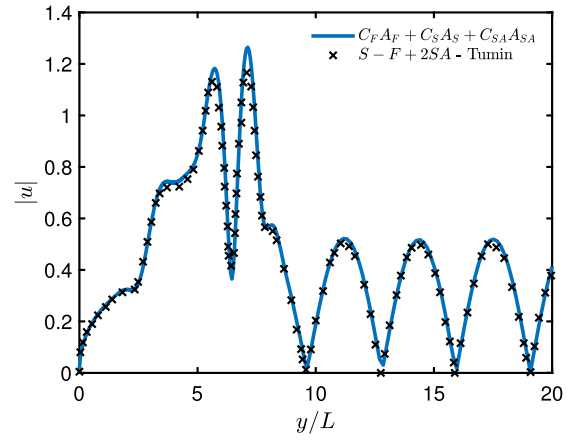

(a) Discrete modes F and S.

(b) Continuous fast and slow acoustic modes.

Fig. 14. Streamwise velocity component of the discrete and continuous mode used for the bi-orthogonal decomposition verification (flat plate, $K = 1$, $M = 5.95$, $T_w/T_{ad} = 0.1$, $F = 10^{-4}$, $Re = 2300$, $\beta = 0.16$).

(a) Superposition of mode S, F, and fast acoustic mode.

(b) Superposition of mode S, F, and slow acoustic mode.

Fig. 15. Reconstructed signal with decomposed coefficients plotted against the original input signal (flat plate, $K = 1$, $M = 5.95$, $T_w/T_{ad} = 0.1$, $F = 10^{-4}$, $Re = 2300$, $\beta = 0.16$).

4.3. Bi-orthogonal eigenfunction system of hypersonic flow over a blunt nose cone

After verifying the eigenfunctions with a case of hypersonic flow over a flat plate, the next step is to develop the bi-orthogonal eigenfunction system for the hypersonic flow over a blunt nose cone and analyze the modal effects. For a weak disturbance, the boundary layer transition is dependent on the initial disturbance amplitude generated by the receptivity of environmental forcing. The current amplitude method by Mack [26] utilizes the initial disturbance amplitude, in the form of receptivity coefficient, as an important parameter to obtain transition predictions. Since the amplitude method relies on the estimated initial and maximum disturbance amplitude to iterate for the transition location, an accurate estimation of the initial amplitude or the receptivity coefficient is crucial. Currently, the receptivity coefficient is obtained either empirically such as in Marineau's work [27] or using a combination of LST and DNS results suggested by Huang and Zhong [28]. In the experimental approach, limited receptivity data is obtained due to the high cost of the experimental procedure for hypersonic flow. The computational procedure used by Huang and Zhong [28] computes the receptivity coefficient with a backtracking procedure that relies heavily on the validation of LST. In this approach, the initial amplitude is obtained with the unstable mode amplitude, $A(s, f_n)$, at a downstream region and the N factor computed by LST or DNS.

$$C_{\text{rec}}(f_n) = A_0(f_n) = \frac{A(s, f_n)}{e^{N(s, f_n)}}, \tag{77}$$

where the term e^N can be obtained with an integration of the spatial growth rate from the neutrally stable location s_0 to an arbitrary location s,

$$N = \int_{s_0}^{s} -\alpha_i \, \mathrm{d}s'. \tag{78}$$

While this procedure is effective in extracting the second mode receptivity coefficient, which is mostly responsible for the breakdown to transition, the amplitude, $A(s, f_n)$, can only be extracted at a location of second mode dominance. To obtain the initial amplitude at the branch I neutral location, backtracking of this second mode amplitude relying on the N factor is required. Hence, this method only approximates the initial amplitude and does not directly compute modal amplitudes at the branch I point. To further improve the accuracy of receptivity data, the bi-orthogonal decomposition is necessary to extract the amplitude of different modes at the branch I location directly. A receptivity simulation case by He and Zhong [4] [19], refer to Case I, is decomposed as an example in this context. The steady meanflow of this case is obtained from a high-order shock-fitting direct numerical simulation in a two-dimensional axis-symmetric grid. In the DNS code, the conservative Navier Stokes equations are transformed into a computational space with the coordinates (ξ, η, ζ). The physical domain is described by a curvilinear grid that matches the geometry of a blunt nose cone with a length of 1.5 m measuring at the centerline. Fig. 16a shows a schematic diagram of the grid over a blunt nose cone. The planar coordinates are deployed instead of cylindrical coordinates in this analysis. The planar coordinates can be implemented in this particular case since the relevant region of interest, including the branch I location, is significantly downstream from the nose region [4]. Hence, a local parallel flow is assumed and the planar coordinates can be utilized for simplification. In cases where the region of interest is near the leading edge, the cylindrical coordinate is recommended to consider curvature effects. Furthermore, due to the axisymmetric nature of the current case, the effects from the azimuthal direction are not investigated. Following this convention, the local Reynolds number defined in Eq. (10) is a function of the dimensional coordinate in meters measured from the leading edge following previous literature [5]. From He and Zhong, the shock is treated as a moving boundary, and the flow condition behind the

Table 2

Freestream Conditions of hypersonic flow over a blunt nose cone following He [4].

R_n (mm)	M_∞	$h_{0,\infty}$ (MJ/kg)	ρ_∞ (kg/m^3)	p_∞ (kPa)	T_∞ (K)	U_∞ (m/s)	$T_w/T_{0,\infty}$	Pr
5.080	9.81	1.06	0.0422	0.64	50.8	1425	0.3	0.72

(a) Computational grid.
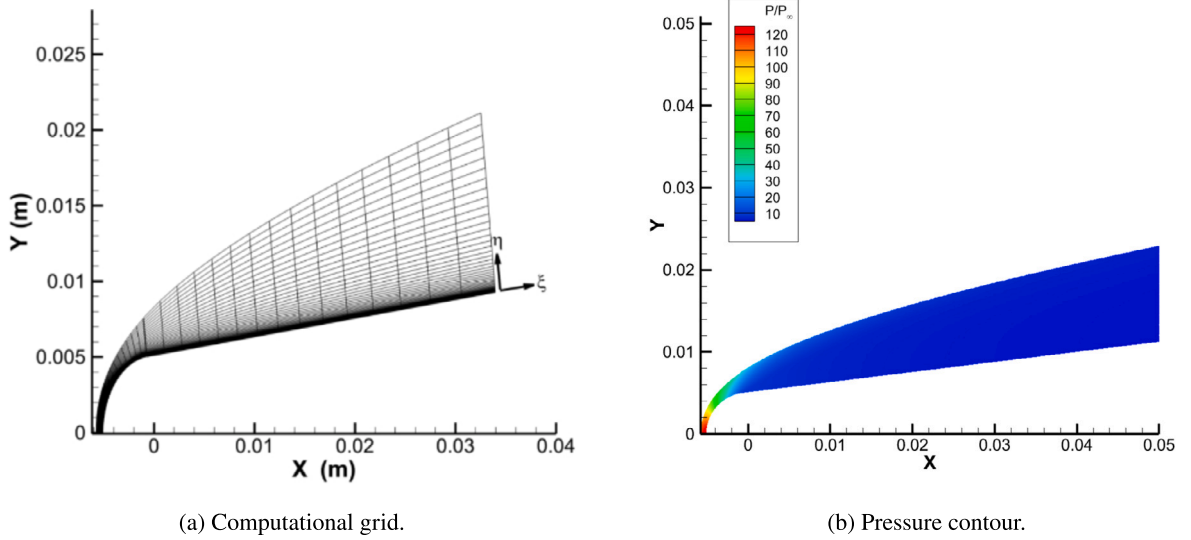
(b) Pressure contour.

Fig. 16. a) Schematic of the computational grid of a blunt cone, adopted from He and Zhong [4] and b) Normalized pressure contour near the blunt nose region. Note that the full domain of the cone ends at the central line distance of $X = 1.5$ m.

shock is determined with the Rankine-Hugoniot relations. The numerical scheme used is a fifth-order upwind scheme for the inviscid fluxes and a sixth-order central scheme for the viscous fluxes. Additional details of the general numerical method used for the DNS simulation and the shock-fitting scheme can be found in Zhong [21]. The steady meanflow parameters for Case I are summarized in Table 2.

Under these flow parameters, the meanflow simulation is conducted from the nose tip towards downstream. Fig. 16b shows the meanflow pressure contour, normalized by the freestream, near the nose region. The pressure contour indicates that the pressure throughout the shock layer is nearly constant downstream from the centerline distance $X = 0.01$ m, which is relatively upstream compared to the full domain length of 1.5 m.

In addition, the meanflow profiles of a selection of normalized streamwise positions, s/R_n, are presented in Fig. 17. The boundary layer near the wall is zoomed whereas the physical shock layer height L is used to non-dimension the wall-normal coordinate. From previous work [4], the most amplified frequency of Case I for various finite pulses (acoustic, temperature, and entropy) is near 190 kHz. From a neutral stability curve by He, the branch I neutral location for such frequency is located near $s/R_n = 130$ or $s^* = 0.66$ m. For the analysis at this location and onward, since the mode shape of the velocity and temperature indicates small variations from Fig. 17, a quasi-parallel assumption is applied such that the meanflow variables are functions of the wall's normal direction coordinate only. Under this assumption, the flowfield data is divided into wall normal snapshots for each streamwise location and each snapshot at these streamwise sampling locations is analyzed.

Following the meanflow simulation, the unsteady simulation is performed to obtain the perturbed flowfield. This unsteady simulation introduces a freestream pulse in front of the blunt nose and the flowfield is recorded as the pulse propagates downstream. Fig. 18 shows a schematic of the disturbance pulse introduced ahead of the cone. During the unsteady simulation, the flowfield data is recorded in various timesteps as the pulse propagates downstream.

The freestream pulse is modeled as a Gaussian pulse [19] and incorporated into the unsteady DNS simulation,

$$q(x, y, z, t) = |q'|_\infty \exp\left(-\frac{(R_c)^2}{2\sigma^2}\right) + q_\infty. \tag{79}$$

The term q is the disturbance variable and $|q'|_\infty$ stands for the peak freestream perturbation. The term R_c refers to the radial distance from the center of the pulse to a point in the flowfield. The variable σ controls both the spatial width of the pulse as well as the frequency bandwidth of the disturbance. The finite spherical pulse parameters and schematic setup for Case I are provided in [19] and [4]. The slow acoustic disturbance in the freestream has a peak density perturbation amplitude, $|\rho'|_\infty$, of 1×10^{-6} as well as a peak pressure perturbation amplitude $|P'|_\infty = |\rho'|_\infty \gamma$. The parameter σ for the finite spherical pulse is set to 1×10^{-3}. The pulse is set to start the advection at a location $x_0 = -0.02$ m with a slow acoustic disturbance speed of $c_\infty = u_\infty - a_\infty$. Fig. 19 presents the unsteady flowfield in the time domain at a downstream region where the second mode instability is dominant. The end of the
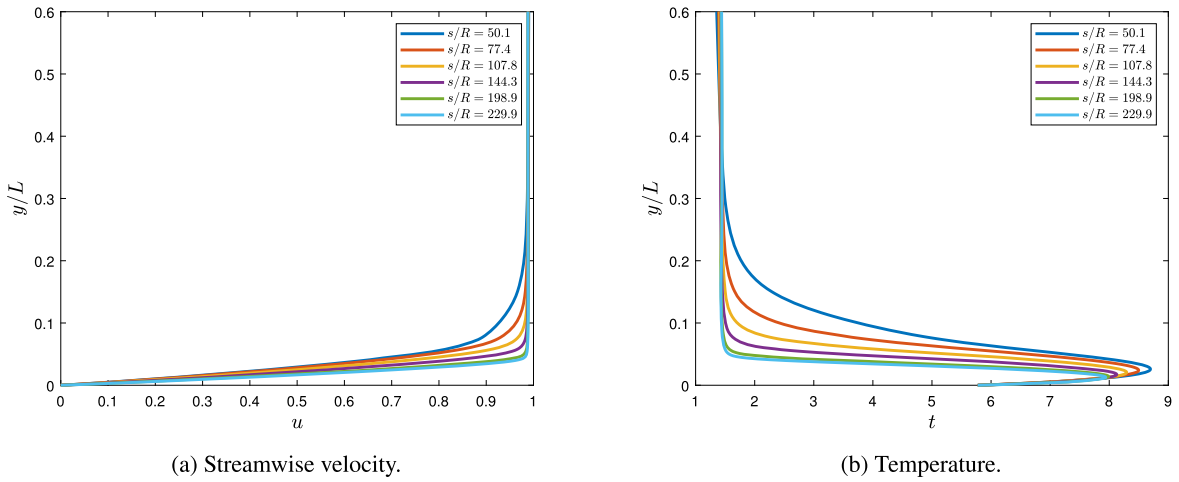
(a) Streamwise velocity.

(b) Temperature.

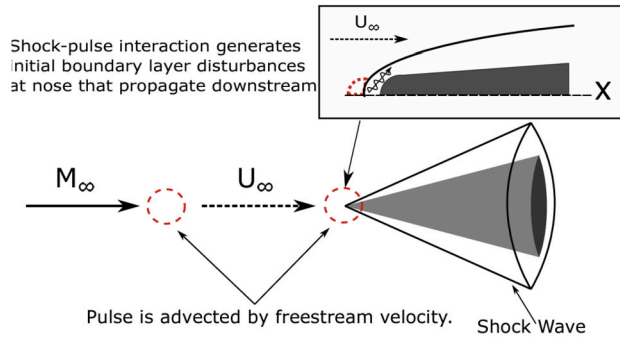**Fig. 17.** Wall normal meanflow profiles along streamwise location s/R_n.

Fig. 18. Schematic diagram of the unsteady simulation set up for a finite spherical pulse disturbance introduced in the freestream, adopted from He and Zhong [4].
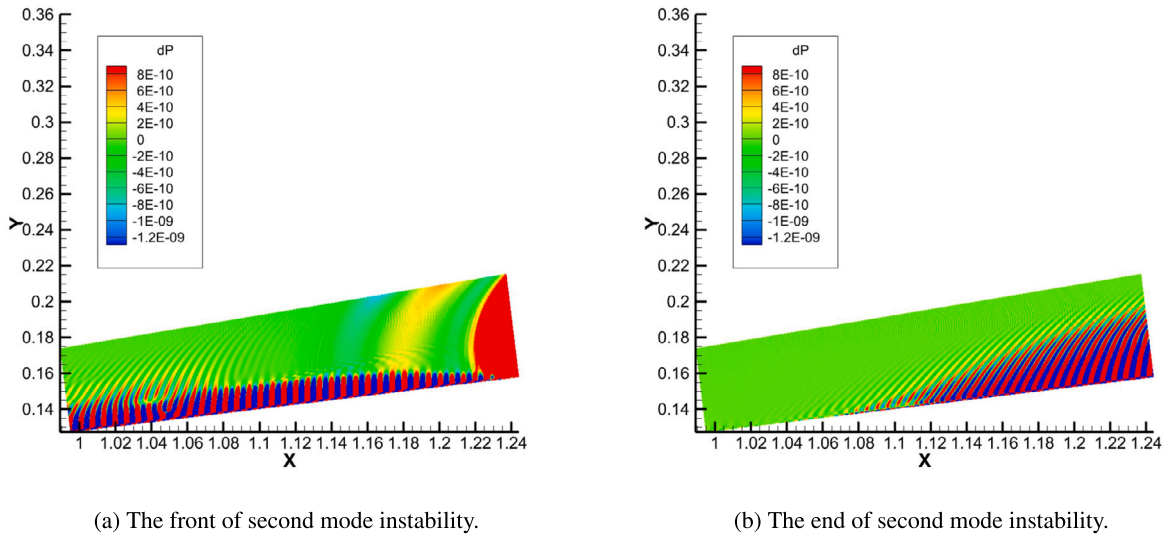

(a) The front of second mode instability.

(b) The end of second mode instability.

Fig. 19. Second mode pressure disturbance in the downstream region following the propagating pulse's end towards the domain's end.

finite pulse is shown in Fig. 19a at the left end of the domain. The distinctive pressure disturbance following the pulse resembles the second mode instability originating from the boundary layer. Furthermore, weaker disturbances radiating from the second mode instability into the rest of the shock layer indicate potential supersonic mode existence [4].
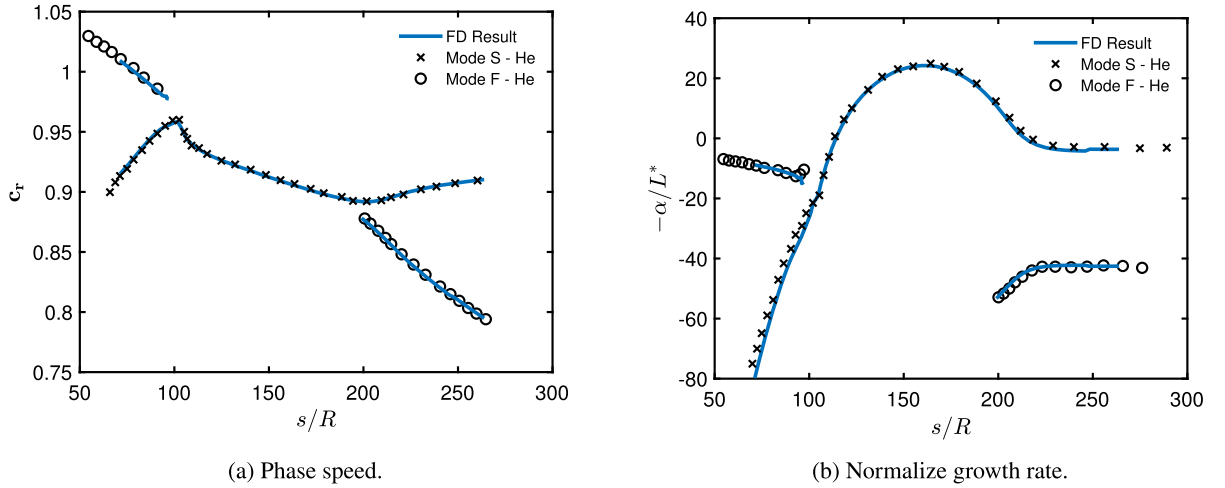
(a) Phase speed.

(b) Normalize growth rate.

Fig. 20. Discrete modes F and S phase speed and growth rate obtained from the finite difference method compared against He and Zhong [4].

To perform the bi-orthogonal decomposition at a streamwise location, the time series snapshots of the wall-normal flowfield at the particular streamwise location are collected. Since the broadband disturbances are modeled using the Gaussian pulse representation, the unsteady flowfield in the time domain is analyzed with Fourier Transform to obtain the disturbance information in the discrete frequency spectrum at the targeted streamwise location. The Fast Fourier Transform (FFT),

$$h\left(t_k\right) \equiv h_k \approx \sum_{n=0}^{N-1} H\left(f_n\right) e^{-2\pi i f_n t_k}, \tag{80}$$

is used to transform all the time-dependent perturbation variables, u, p, v, ρ. The perturbation variables are inputted as $h(t_k)$ and outputted as the complex coefficient $H(f_n)$ for the n_{th} frequency in a total of N discrete frequencies. The complex coefficient $H(f_n)$ is then used as the disturbance input, $\mathbf{z_D}$, to the bi-orthogonal decomposition system for the n_{th} frequency. A sample of the Fourier transformed flowfield at the streamwise locations $s^* = 1.25$ m is plotted against the decomposed result in the latter section. With the FFT perturbation data at a specific frequency, a projection onto the discrete and continuous modes can be performed.

4.3.1. Discrete modes

To verify the accuracy of the result, the discrete mode phase speed and the growth rate over a range of streamwise locations obtained using the high-order finite difference methods are plotted against the results from He and Zhong [19], [4] in Fig. 20. The local spatial eigenvalues results of each location from the spatial analysis are used to derive the local phase speed of a disturbance. Following He and Zhong [4], the phase speed and growth rate for a 200 kHz disturbance is plotted. This disturbance was chosen due to the significant modal amplification suggested by He and Zhong from the Fourier decomposition of the DNS flowfield. For the streamwise calculation of the phase speed and growth rate, an 11 points finite difference scheme is used with the number of grid points $N = 204$. This results in a sparse linear operator in comparison to the spectral collocation method and significantly lowers the computational time when a large number of locations is analyzed.

With a slight mismatch of the upstream mode S growth rate, the result of the finite difference method confirms with previous spectral collocated LST results obtained by He and Zhong. The discrepancy in the upstream mode S growth rate is due to the grid sensitivity of the numerical solution. Yet, overall experiments showed trends closely matching with the reference. Both discrete modes trace back to the originating continuous fast and slow acoustic branches with the phase speeds of $1 + 1/M_\infty$ and $1 - 1/M_\infty$ going upstream. Furthermore, the finite difference result confirms that the synchronization between discrete modes F and S happens near the location of $S/R = 100$ as expected. Another note is that near the synchronization region, the weaker discrete mode in general will be difficult to resolve numerically due to the similarity in the wavenumber [15] [45]. After the verification of the eigenvalues, the eigenfunctions can also be examined. Fig. 21a shows the pressure eigenfunction comparison against the Case I results obtained with LST using spectral collocation method at the streamwise location of $s^* = 1.25$ m and a frequency of 260 kHz. Figs. 21b and 21c are the streamwise velocity and temperature profiles for the discrete modes F and S of the same case. L denotes the length from the wall to the shock here. From the comparison, the pressure eigenfunction results for both discrete modes F and S align well with the reference. The oscillation of the mode F eigenfunction near the temperature critical region $y/L \approx 0.06$ from the reference is smoothed out in the finite difference result.

Numerical experiments also showed that the oscillation in the reference is an effect of the sensitivity to the grid distribution as different grid distributions can produce different oscillation amplitudes in the region. This sensitivity can be due to slight non-parallel effects since this behavior is not recorded for the flat plate cases. Looking at the streamwise velocity and temperature components, two critical layers can also be identified. The location of the temperature critical layer in the discrete mode S aligns with the meanflow
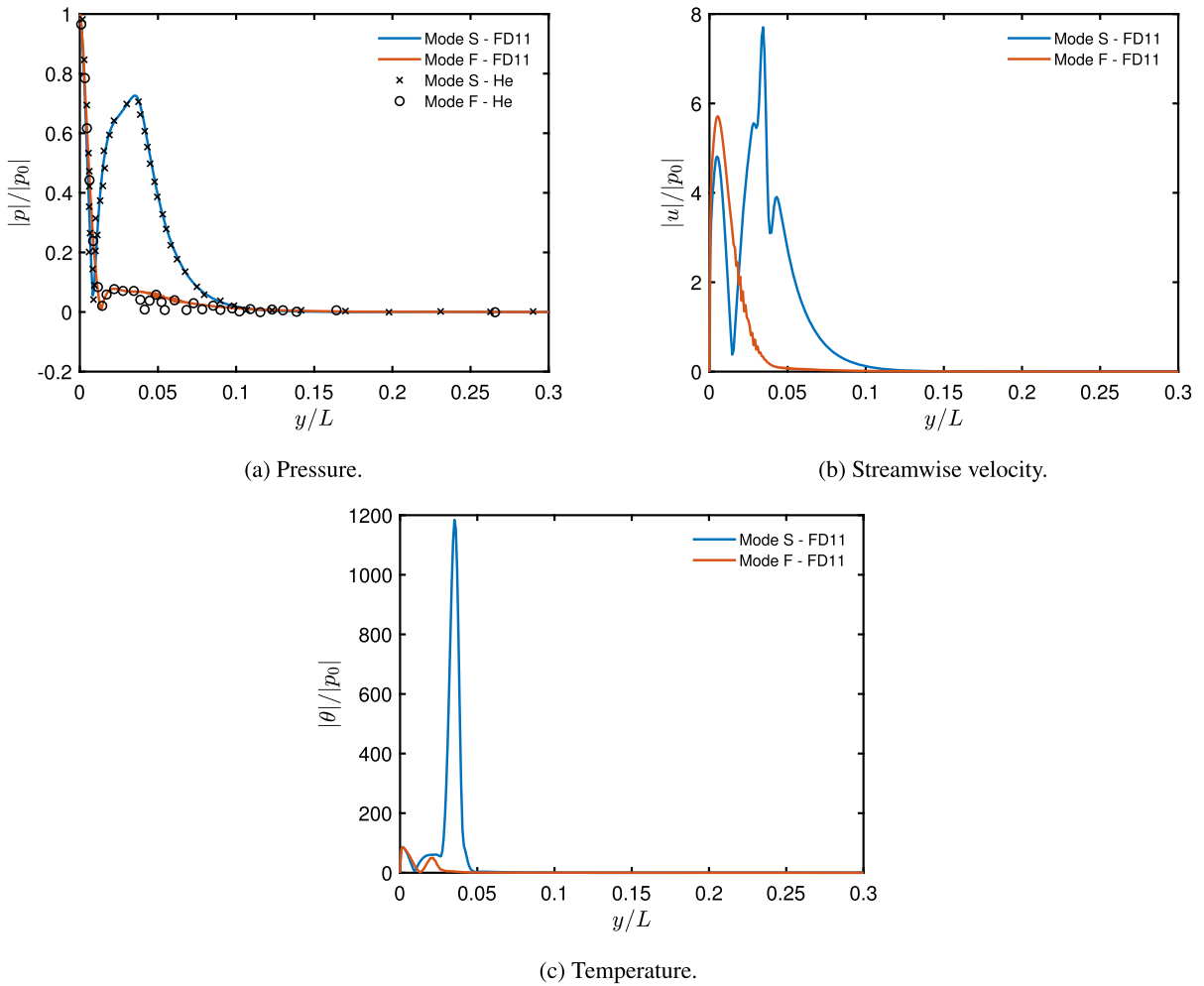
(a) Pressure.

(b) Streamwise velocity.

(c) Temperature.

Fig. 21. Discrete modes F and S pressure (comparison against He and Zhong [19]), streamwise velocity and temperature eigenfunctions.

profiles shown in [4]. In this case, a well-distributed grid is necessary to resolve the critical layers since the solution is more sensitive to the grid. Moreover, the second mode dominance is clearly shown in the higher amplitudes of perturbation variable eigenfunctions.

4.3.2. Continuous modes

After the verification of the discrete mode, the continuous spectrum should be investigated. The finite difference scheme used to obtain the continuous modes has a stencil length of 11 with 404 grid points. The snapshot at the streamwise location of $s^* = 1.25$ m and a frequency of 200 kHz is used as a sample case. The continuous mode eigenfunction results presented below have the value K set to 1, showing only one location of the continuous branch. The freestream boundary conditions are applied behind the bow shock to include all changes in the shock layer. From previous studies [16] [34] [44], the vorticity and entropy modes have been concluded to have a small contribution to the boundary layer flow. This is due to the rapid decay of the modes after the shock and not penetrating the boundary layer [16]. Fig. 22 shows the behavior of the vorticity and entropy mode.

The results indicate that, at the end of the boundary layer, $y/L = 0.2$, both the vorticity and entropy mode have large freestream oscillations that do not penetrate the boundary layer edge as mentioned above. On the other hand, the fast and slow acoustic modes have significant perturbations inside the boundary layer compared to the freestream. Fig. 23 presents the fast acoustic mode velocity and pressure compared with results obtained with the integration method used by Tumin [16] and Miselis [34]. In this demonstration, instead of a pressure normalization, the streamwise velocity gradient, du/dy, is used to normalize the eigenfunctions as well. The results obtained with Tumin's method are resolved with $N = 3000$ grid points and the Gram-Schmidt orthonormalization was performed at each step. The overall result demonstrates agreement with both the behavior of a freestream non-decaying continuous mode and the integration result. Furthermore, Fig. 23a also shows an eigenfunction obtained with an interrupted meanflow having a domain of $y/L = 0$ to 0.07. From Fig. 17, the meanflow has its gradients before $y/L = 0.07$ and this result shows that as long as the high gradient region is included in the domain, the eigenfunctions can be resolved.

Furthermore, since the K value can be interpreted as a wavenumber in the wall-normal direction, Fig. 24 shows the slow acoustic mode eigenfunction evaluated at a discrete K value of 0.5 to examine the behavior with varying wavenumber. From the
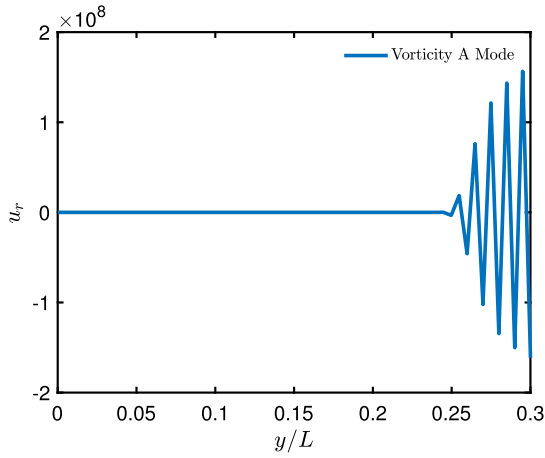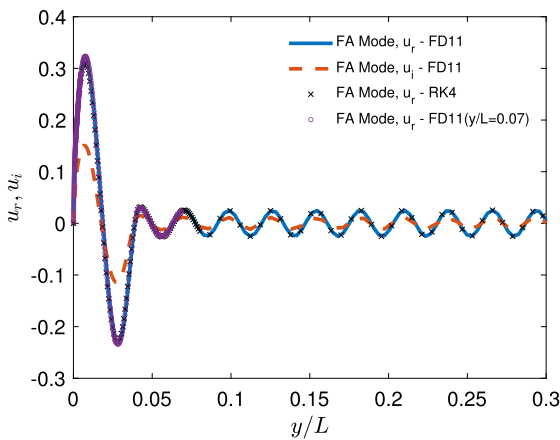
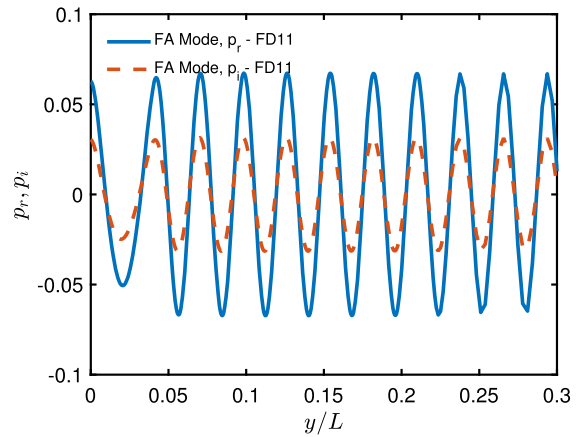(a) Vorticity A mode eigenfunction.
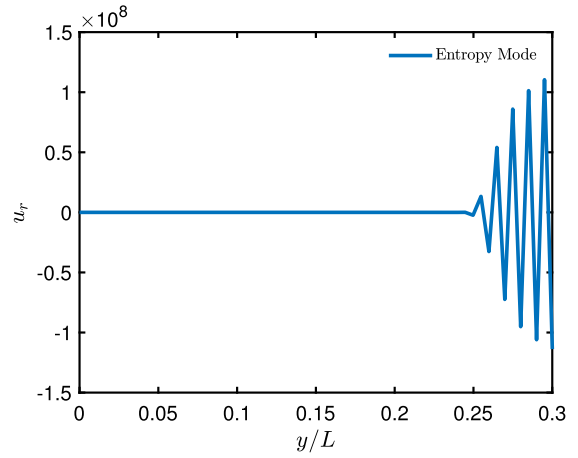
(b) Entropy mode eigenfunction.

Fig. 22. Vorticity A and entropy mode results obtained with finite difference method.

(a) Fast acoustic mode streamwise velocity eigenfunction.

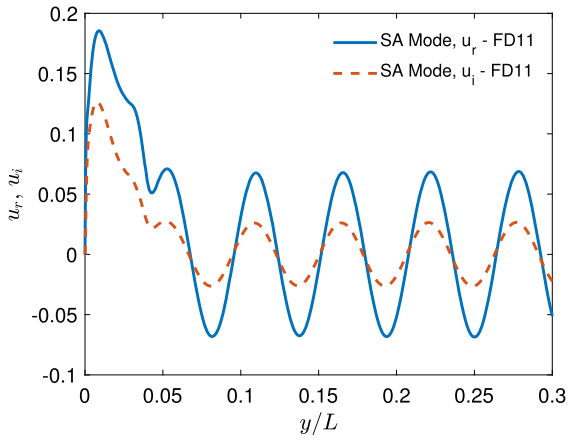(b) Fast acoustic mode pressure eigenfunction.

Fig. 23. Fast acoustic mode results obtained with finite difference compared with results obtained from Tumin's method.

eigenfunction, when the K value is lowered to 0.5, which is closer to the branch point, the continuous oscillations propagate onto the freestream with longer wavelengths.
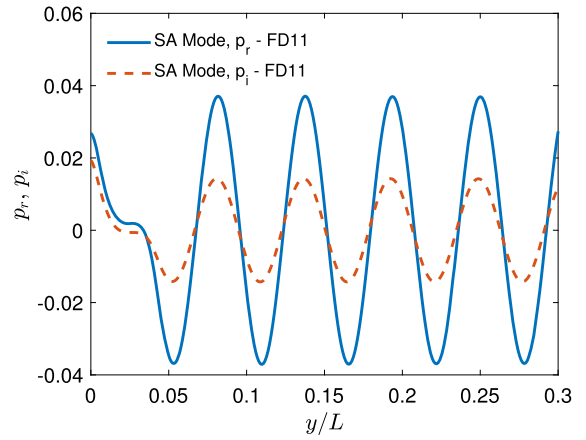
4.3.3. Bi-orthogonal decomposition

With the developed discrete and continuous modes, the bi-orthogonal decomposition verification procedure is the same as the flat plate case. An arbitrary disturbance is composed of the direct discrete and continuous modes. The same location and flow conditions are set as the above verification steps. For the continuous mode decomposition, only the fast and slow acoustic modes are considered since the vorticity and entropy modes do not penetrate the boundary layer. Since the continuous mode is discretized with distinct K values, only one location in each continuous branch is included in the design of the arbitrary signal to eliminate the non-orthogonality effect of the same branch. Fig. 25 shows the streamwise velocity result of an arbitrary signal made up of a combination of mode S, F, and fast acoustic mode with $C_S = 1$, $C_F = -1$, $C_{FA,K=0.5} = -2$. Another case of an arbitrary signal made up of a combination of mode S, F, and slow acoustic mode with $C_S = 1$, $C_F = -1$, $C_{SA,K=0.5} = -2$ is shown in Fig. 26. The blue lines show the reconstructed streamwise velocity and temperature components combined with the different discrete/continuous modes and coefficients resulting from the bi-orthogonal decomposition. The black markers indicate the arbitrarily designed perturbation.

The bi-orthogonal decomposition of the arbitrary perturbation shown in Fig. 25 results in coefficients of $C_S = 9.9976 \times 10^{-1} - 5.6270 \times 10^{-3}i$, $C_F = -1.0009 - 3.6908 \times 10^{-2}i$, and $C_{FA,K=0.5} = -1.9998 - 8.1469 \times 10^{-5}i$. The largest relative error to the original coefficient is around 3.7 percent. Moreover, the coefficients of the discretized slow acoustic branch have a maximum magnitude in the order of 10^{-3}. The second decomposition example in Fig. 26 has similar results as well. The resulting coefficients are $C_S = 9.99986 \times 10^{-1} - 5.1401 \times 10^{-4}i$, $C_F = -1.0008 + 1.1651 \times 10^{-3}i$, and $C_{FA,K=0.5} = -2.000 + 2.8032 \times 10^{-6}i$. The coefficients for the other branch have the magnitudes of 10^{-3} as well.
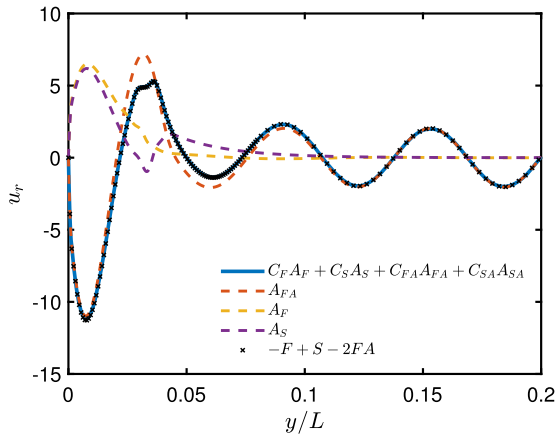
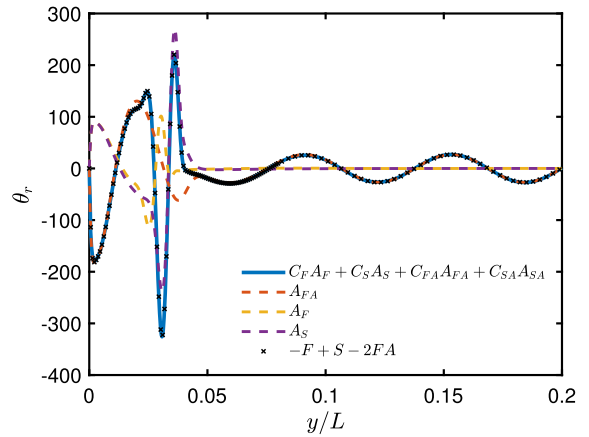(a) Slow acoustic mode streamwise velocity eigenfunction.

(b) Slow acoustic mode pressure eigenfunction.

Fig. 24. Slow acoustic mode results obtained with the finite difference method, evaluated at $K = 0.5$.
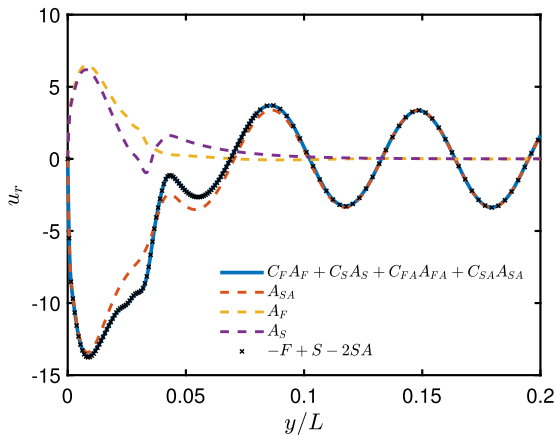

(a) Streamwise velocity.

(b) Temperature.

Fig. 25. Bi-orthogonal decomposition verification of the blunt nose cone case with discrete modes and fast acoustic continuous mode.
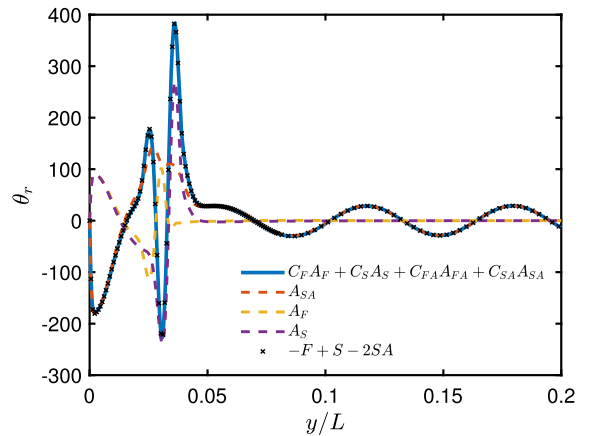

(a) Streamwise velocity.

(b) Temperature.

Fig. 26. Bi-orthogonal decomposition verification of the blunt nose cone case with discrete modes and slow acoustic continuous mode.

(a) Streamwise Velocity results.

(b) Pressure results.
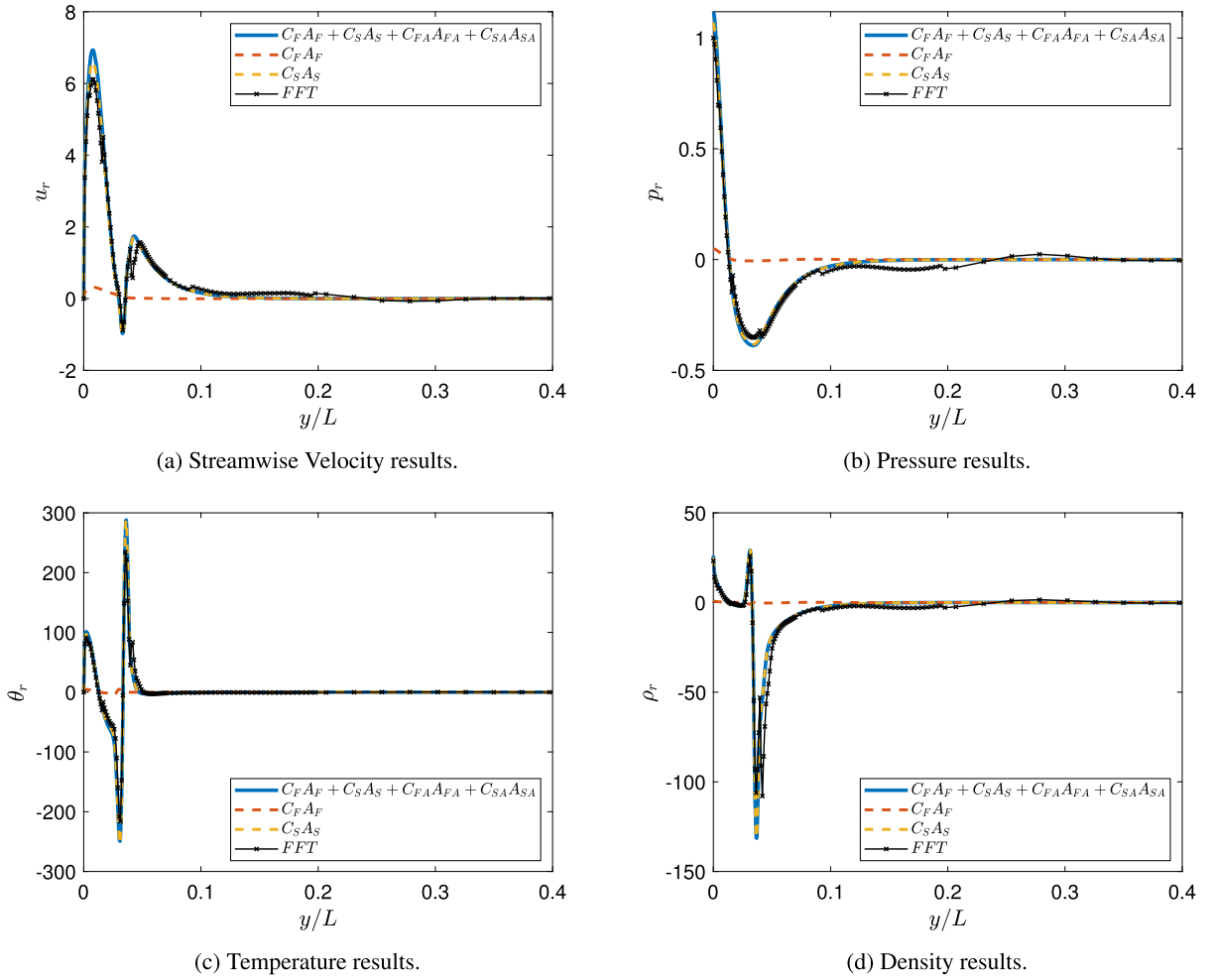
(c) Temperature results.

(d) Density results.

Fig. 27. Real component of the streamwise velocity component, pressure, temperature, and density projection results obtained with finite difference compared with the original FFT data.

After the verification of bi-orthogonality between discrete and continuous modes, the unsteady receptivity flowfield of a finite spherical slow acoustic pulse is decomposed to obtain the coefficients of modal influence for each mode. For demonstration purposes, the Case I disturbance flowfield at a streamwise location $s^* = 1.25$ m with a frequency of 200 kHz is projected to the discrete and continuous modes in Fig. 27. This streamwise location is chosen since the discrete mode S is dominant while the influence from other modes is less significant. The decomposition would be valid if the resulting mode S coefficient is dominant compared with other modes. Furthermore, a snapshot of the wall-normal flow profile is used as the perturbation flowfield since the flow is nearly parallel and axisymmetric in the azimuthal direction. In this decomposition, each continuous branch is discretized with a $\Delta K = 0.01$ for a range of values of $K = 0$ to 4. At this streamwise location, a band of frequencies from 160 to 200 kHz exhibits high amplification in the surface pressure indicating a second mode response on the neutral curve [4]. Hence, the discrete modes F and S contribution are also plotted for comparison. From Fig. 27, the FFT data aligns closely with both the discrete mode S and the projection result as expected. Moreover, from both the streamwise velocity and the pressure perturbation, the mode shape of the discrete mode S matches better in the region below $y/L = 0.02$. This is due to a dominant behavior of the discrete mode S while the projection result might have included numerical errors during the numerical integration in the decomposition process. In this case, the theoretical modal coefficient for discrete mode S should be $|C_S| = 1$, however, the numerical result yields $|C_S| = 1.0685$ which includes a 6.85 percent relative error. Furthermore, the projection result also includes small magnitudes of numerical errors from other modes such as the discrete mode F, $|C_F| = 4.06 \times 10^{-2}$. These additional numerical errors accumulate and result in a slight misalignment when all modal influences are superposed to reconstruct the signal. Improvements such as higher-order numerical integration can be deployed in the future to minimize the error. Since the result is obtained by decomposing the whole wall-normal profile up to the shock, an additional decomposition up to the boundary layer edge is performed and the discrete mode S coefficient obtained is within 1 percent margin from the full domain decomposition. Note that this might not be the case if the decomposition is performed at the branch I neutral location since features such as Mach wave can exist outside of the boundary layer. Moreover, the oscillation in the streamwise velocity and pressure components near $y/L = 0.2$ to 0.4, however, is not an effect of the oscillating continuous modes
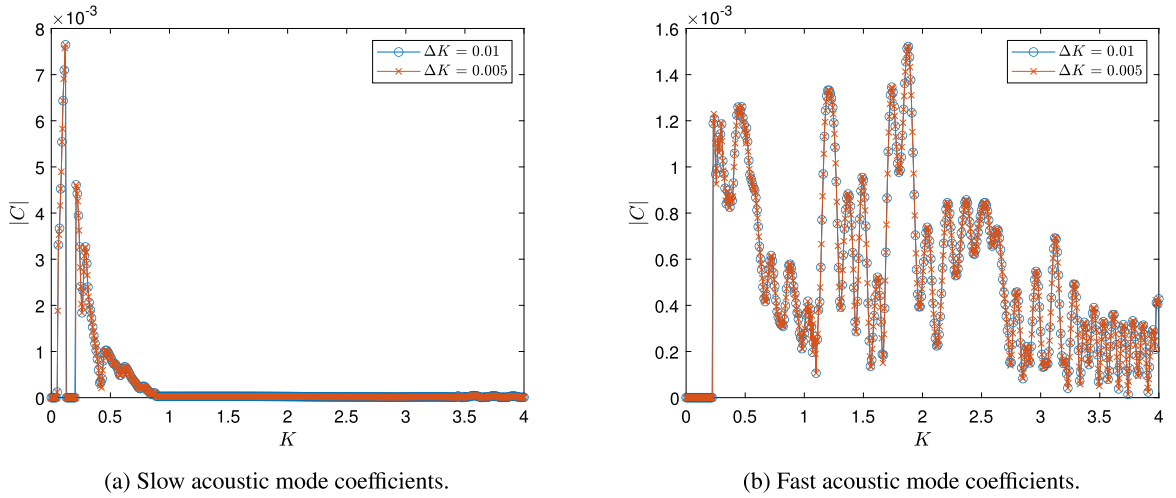
(a) Slow acoustic mode coefficients.

(b) Fast acoustic mode coefficients.

Fig. 28. The magnitude of projected coefficients of the slow acoustic and fast acoustic continuous modes.

since the oscillation does not propagate through the freestream. This might be a contribution to the non-modal/transient effects as the discrete mode S is near the slow acoustic branch at this streamwise location [4].

The coefficients of the two continuous modes for a range of K values from 0 to 4 are also plotted in Fig. 28. Two different $\Delta K = 0.01$ and 0.005 values are deployed for validation purposes. Results obtained with the two values align well with each other, showing a grid convergence on the K distribution. Both the slow acoustic and fast acoustic continuous branches have the largest coefficients in the K value range from 0 to 2 which follows the overall trend of the influence of continuous branches presented by Tumin [15] and Miselis [34]. Yet, in Fig. 28b, there exist oscillations that can be due to numerical errors during the integration. Since this paper is a demonstration of the concept, further research on reducing the numerical error would be beneficial.

For further investigations in non-modal effects, the input-output analysis mentioned above can also be used in parallel to verify the result. In addition, Nichols and Candler's computed result of input-output analysis for a hypersonic boundary layer also captures similar non-modal oscillations in mode amplitude which are attributed to energy exchange between modes [39]. The FFT data is also projected onto the vorticity and entropy modes for verification. The coefficients of both modes have a magnitude of 10^{-7} which confirms with the previous studies that these modes do not penetrate the boundary layer [16] [34]. Knowing the contribution of each mode, various stability analysis methods, such as receptivity coefficients calculation and Mack's amplitude method [26], can be applied in extension.

5. Conclusions

This paper presents a new general very high-order (10 or higher to spectral-like) finite difference scheme on a non-uniform grid for linear stability theory and bi-orthogonal decomposition. This new method offers a unified numerical framework to efficiently compute both discrete and continuous mode eigenfunctions, which can be seamlessly incorporated into Tumin's bi-orthogonal decomposition framework [16]. Using the boundary value problem approach, the method implementation eliminates the need for the intricate Gram-Schmidt orthonormalization and the associated recovery process in the initial value problem approach. Different boundary conditions for the finite difference method are adapted to compute both discrete and continuous modes depending on the eigenvalue characteristics. For discrete modes, the global eigenvalue decomposition and the local spatial eigenvalue search can be performed with minimal modification to wall boundary conditions. For continuous modes, the asymptotic boundary condition by the means of freestream fundamental solution is utilized to obtain the eigenfunctions with similar eigenvalues, which correspond to the continuous vorticity and entropy modes. For the fast and slow acoustic modes, characterized by distinct eigenvalues, both the asymptotic boundary condition and a simple extrapolation can be sufficient to obtain these modes. Furthermore, these finite difference operators can be tailored to have sparse structure or spectral-like resolution, depending on the length of the finite difference stencil. Moreover, the finite difference method leverages a non-uniform grid distribution with multi-domains to ensure high-order accuracy with stability and bypass the grid transformation procedure needed for the collocation methods.

The new numerical method has demonstrated its effectiveness in two flow scenarios: a hypersonic flow over a flat plate and a blunt nose cone. Both the discrete and continuous modes computed using the new method have been rigorously validated through comparisons with established studies of hypersonic flow over a flat plate and hypersonic flow over a blunt nose cone. The results obtained for both discrete and continuous modes in the flat plate case exhibit close agreement with prior investigations conducted by Tumin [16], Miselis [34], and Balakumar [44]. Subsequently, the bi-orthogonal decomposition for the hypersonic flow over a flat plate has also been performed on a designed disturbance with known coefficients. The recovered amplitude coefficients with the bi-orthogonal decomposition also match closely with the assigned coefficients, affirming the orthogonality between the resulting modes.

Furthermore, the new method was employed to study the receptivity of a hypersonic flow over a blunt nose cone. The bi-orthogonal eigenfunction system of discrete and continuous modes has been computed using the new method for the hypersonic flow over a blunt nose cone based on the steady DNS meanflow data provided by He and Zhong [19]. The computed discrete mode phase speed and growth rate aligned well with previous results in He's work. The eigenfunctions of the discrete modes also compared well with critical layers adequately resolved. Furthermore, the continuous modes obtained with the new method also displayed behaviors consistent with the physics. The bi-orthogonal decomposition of the unsteady DNS flowfield data stemming from a freestream receptivity simulation by He and Zhong [19] also has been performed with preliminary results shown. This procedure involved applying the orthogonality relation to Fourier-transformed flowfield data at a specified frequency. By projecting the perturbation variables onto the bi-orthogonal eigenfunctions, the modal perturbation amplitudes can be obtained. Remarkably, the decomposition results aligned with the observation of the discrete mode S being dominant in the second mode instability region.

Given that this paper predominantly focuses on presenting the new numerical procedure, the immediate next step of this research will be the application of the newly developed method to obtain the receptivity data at the branch I neutral location. The bi-orthogonal decomposition is particularly useful in the freestream receptivity study of hypersonic flow over a blunt body for a better understanding of the dominant source of the disturbance. Since the amplitude method by Mack [26] relies on an accurate initial disturbance amplitude to predict the transition location, the modal decomposition of the initial perturbation, using the discrete and continuous modes computed by the new method, is urgent in the subsequent step of research. Moreover, given the diversity of freestream disturbances such as acoustic/entropy/vorticity and turbulence, which leads to different instability behavior, the accurate evaluation of discrete and continuous modes using this new method allows further application of decomposition to examine modal contributions [19]. In addition to freestream receptivity, the further application of bi-orthogonal decomposition for blowing and suction can be investigated for the decomposition effectiveness of the current bi-orthogonal system to forced receptivity. Moreover, this tool of general very high-order accuracy can be extended to different flow scenarios, including real gas flow and other geometry to build a more physically representative model and better reveal the characteristics in the study of hypersonic boundary layer transition.

CRediT authorship contribution statement

Zihao Zou: Conceptualization, Data curation, Formal analysis, Investigation, Methodology, Software, Validation, Visualization, Writing – original draft, Writing – review & editing. **Xiaolin Zhong:** Funding acquisition, Project administration, Resources, Supervision, Writing – review & editing.

Declaration of competing interest

The authors declare the following financial interests/personal relationships which may be considered as potential competing interests: Zihao Zou reports financial support was provided by UCLA. If there are other authors, they declare that they have no known competing financial interests or personal relationships that could have appeared to influence the work reported in this paper.

Data availability

Data will be made available on request.

Appendix A. The matrix elements

The matrix elements of **H** in Eq. (15) are presented here. Similar to Ref. [34] [16], the convention is to define $r = 2(\epsilon + 2)/3$ and $m = 2(\epsilon - 1)/3$ where ϵ is the ratio of bulk viscosity to dynamic viscosity and equals to 0 following Stoke's hypothesis. For entries not specified, the coefficients are equal to zero. We first define,

$$\chi = \left[\frac{Re}{\mu} - \frac{i\hat{\omega} r}{P} \right]^{-1} \tag{81}$$
$$\hat{\omega} = \omega - \alpha U.$$

For **H**, we have

$$H^{1,2} = 1$$
$$H^{2,1} = \alpha^2 + \beta^2 - i\hat{\omega} P \gamma M^2 \frac{Re}{\mu T}$$
$$H^{2,2} = -\frac{1}{\mu} \frac{\partial \mu}{\partial y}$$
$$H^{2,3} = -i\alpha(m+1)\frac{1}{T}\frac{\partial T}{\partial y} - i\alpha \frac{1}{\mu}\frac{\partial \mu}{\partial y} + \mathrm{Re}\, P\gamma M^2 \frac{1}{\mu T}\frac{\partial U}{\partial y} + i\alpha(m+1)\frac{1}{P}\frac{\partial P}{\partial y}$$
$$H^{2,4} = i\alpha \frac{Re}{\mu} + \alpha\hat{\omega}(m+1)\frac{1}{P}$$

$$H^{2,5} = -\alpha\hat{\omega}(m+1)\frac{1}{T} - \frac{1}{\mu}\left(\frac{\partial T}{\partial y}\frac{\partial U}{\partial y}\frac{\partial^2\mu}{\partial T^2} + \frac{\partial\mu}{\partial T}\frac{\partial^2 U}{\partial y^2}\right)$$

$$H^{2,6} = -\frac{1}{\mu}\frac{\partial\mu}{\partial T}\frac{\partial U}{\partial y}$$

$$H^{3,1} = -i\alpha$$

$$H^{3,3} = \frac{1}{T}\frac{\partial T}{\partial y} - \frac{1}{P}\frac{\partial P}{\partial y}$$

$$H^{3,4} = \frac{i\hat{\omega}}{P}$$

$$H^{3,5} = -\frac{i\hat{\omega}}{T}$$

$$H^{3,7} = -i\beta$$

$$H^{4,1} = -i\chi\alpha\left(r\frac{1}{T}\frac{\partial T}{\partial y} + \frac{2}{\mu}\frac{\partial\mu}{\partial y} - r\frac{1}{P}\frac{\partial P}{\partial y}\right)$$

$$H^{4,2} = -i\chi\alpha$$

$$H^{4,3} = \chi\left(-\alpha^2 - \beta^2 + i\hat{\omega}P\gamma M^2\frac{Re}{\mu T} + r\frac{1}{T}\frac{\partial^2 T}{\partial y^2} + r\frac{1}{\mu T}\frac{\partial\mu}{\partial y}\frac{\partial T}{\partial y} - r\frac{1}{\mu P}\frac{\partial\mu}{\partial y}\frac{\partial P}{\partial y} + 2r\frac{1}{P^2}\left[\frac{\partial P}{\partial y}\right]^2 - 2r\frac{1}{PT}\frac{\partial P}{\partial y}\frac{\partial T}{\partial y} - r\frac{1}{P}\frac{\partial^2 P}{\partial y^2}\right)$$

$$H^{4,4} = -i\chi r\frac{1}{P}\left(\alpha\frac{\partial U}{\partial y} - \hat{\omega}\frac{1}{T}\frac{\partial T}{\partial y} - \hat{\omega}\frac{1}{\mu}\frac{\partial\mu}{\partial y} + 2\hat{\omega}\frac{1}{PT}\frac{\partial P}{\partial y}\right)$$

$$H^{4,5} = i\chi\left(\alpha r\frac{1}{T}\frac{\partial U}{\partial y} + \alpha\frac{1}{\mu}\frac{\partial\mu}{\partial T}\frac{\partial U}{\partial y} - r\hat{\omega}\frac{1}{\mu T}\frac{\partial\mu}{\partial y} + r\hat{\omega}\frac{1}{PT}\frac{\partial P}{\partial y}\right)$$

$$H^{4,6} = -i\chi r\hat{\omega}\frac{1}{T}$$

$$H^{4,7} = -i\chi\beta\left(r\frac{1}{T}\frac{\partial T}{\partial y} + 2\frac{1}{\mu}\frac{\partial\mu}{\partial y} - r\frac{1}{P}\frac{\partial P}{\partial y}\right)$$

$$H^{4,8} = -i\chi\beta$$

$$H^{5,6} = 1$$

$$H^{6,2} = -2(\gamma-1)M^2\Pr\frac{\partial U}{\partial y}$$

$$H^{6,3} = -2i\alpha(\gamma-1)M^2\Pr\frac{\partial U}{\partial y} + P\gamma M^2\Pr\frac{Re}{\mu T}\frac{\partial T}{\partial y} - (\gamma-1)M^2\Pr\frac{Re}{\mu}\frac{\partial P}{\partial y}$$

$$H^{6,4} = i\hat{\omega}(\gamma-1)M^2\Pr\frac{Re}{\mu}$$

$$H^{6,5} = \alpha^2 + \beta^2 - i\hat{\omega}\Pr M^2\Pr\frac{Re}{\mu T} - (\gamma-1)M^2\Pr\frac{1}{\mu}\frac{\partial\mu}{\partial T}\left(\frac{\partial U}{\partial y}\right)^2 - \frac{1}{\mu}\frac{\partial^2\mu}{\partial y^2}$$

$$H^{6,6} = -\frac{2}{\mu}\frac{\partial\mu}{\partial y}$$

$$H^{7,8} = 1$$

$$H^{8,3} = -i\beta(m+1)\frac{1}{T}\frac{\partial T}{\partial y} - i\beta\frac{1}{\mu}\partial\mu\partial y + i\beta(m+1)\frac{1}{P}\frac{\partial P}{\partial y}$$

$$H^{8,4} = \beta\hat{\omega}(m+1)\frac{1}{P} + i\beta\frac{Re}{\mu}$$

$$H^{8,5} = -\beta\hat{\omega}(m+1)\frac{1}{T}$$

$$H^{8,7} = \alpha^2 + \beta^2 - i\hat{\omega}P\gamma M^2\frac{Re}{\mu T}$$

$$H^{8,8} = -\frac{1}{\mu}\frac{\partial\mu}{\partial y}$$

Appendix B. Asymptotic fundamental solutions

Solving the characteristic equation of Eq. (20), the asymptotic solutions $\mathbf{z}_{\alpha\beta_0}^{(\mathbf{m})}$ can be derived and results agreed with [16]. First, we define

$$b_{11} = H^{21}$$
$$b_{22} = H^{42}H^{24} + H^{43}H^{34} + H^{46}H^{64} + H^{48}H^{84}$$
$$b_{23} = H^{42}H^{25} + H^{43}H^{35} + H^{46}H^{65} + H^{48}H^{85}$$
$$b_{32} = H^{64}, b_{33} = H^{65},$$

(82)

where H^{ij} are the components of the coefficient matrix $\mathbf{H}$ from Eq. (15). Subsequently, the eigenvalue λ_m with subscript $m = 1, \cdots, 8$ denoting the mth eigenvalue is

$$(\lambda_m)^2 = b_{11} = \alpha^2 + \beta^2 + \mathrm{i}\,\mathrm{Re}(\alpha - \omega), \quad m = 1, 2, 7, 8$$
$$(\lambda_m)^2 = (b_{22} + b_{33})/2 + \frac{1}{2}\sqrt{(b_{22} - b_{33})^2 + 4b_{23}b_{32}}, \quad m = 3, 4$$
$$(\lambda_m)^2 = (b_{22} + b_{33})/2 - \frac{1}{2}\sqrt{(b_{22} - b_{33})^2 + 4b_{23}b_{32}}, \quad m = 5, 6.$$

(83)

With the first two pairs of freestream eigenfunctions,

$$\mathbf{z}_{\alpha\beta_0}^{(\mathbf{m})} = \left(1, \lambda_m, H^{31}/\lambda_m, 0, 0, 0, 0, 0\right)^T, \quad m = 1, 2$$
$$\mathbf{z}_{\alpha\beta_0}^{(\mathbf{m})} = \left(0, 0, H^{37}/\lambda_m, 0, 0, 0, 1, \lambda_m\right)^T, \quad m = 7, 8,$$

(84)

where matrix element H^{31} is $-\mathrm{i}\alpha$ representing $\partial/\partial x$ and H^{37} is $-\mathrm{i}\beta$ representing $\partial/\partial z$. For $(\mathbf{z}_{\alpha\beta_0}^{(\mathbf{m})})_k$ with $m = 3, 4, 5, 6$ being the mth eigenvector and k being the kth component of the mth vector, the eigenvectors are

$$\mathbf{z}_{\alpha\beta_0}^{(\mathbf{m})} = \begin{bmatrix} 1 \\ \lambda_m \\ \left(H^{31}\left(\mathbf{z}_{\alpha\beta_0}^{(\mathbf{m})}\right)_1 + H^{34}\left(\mathbf{z}_{\alpha\beta_0}^{(\mathbf{m})}\right)_4 + H^{35}\left(\mathbf{z}_{\alpha\beta_0}^{(\mathbf{m})}\right)_5 + H^{37}\left(\mathbf{z}_{\alpha\beta_0}^{(\mathbf{m})}\right)_7\right)/\lambda_m \\ (\lambda_m^2 - H^{21})b_{23}/b_{12} \\ -(b_{22} - \lambda_m^2)(\lambda_m^2 - H^{21})/b_{12} \\ \lambda_m\left(\mathbf{z}_{\alpha\beta_0}^{(\mathbf{m})}\right)_5 \\ \left(H^{84}\left(\mathbf{z}_{\alpha\beta_0}^{(\mathbf{m})}\right)_4 + H^{85}\left(\mathbf{z}_{\alpha\beta_0}^{(\mathbf{m})}\right)_5\right)/\left(\lambda_m^2 - H^{87}\right) \\ \lambda_m\left(\mathbf{z}_{\alpha\beta_0}^{(\mathbf{m})}\right)_7 \end{bmatrix}$$

(85)

where $b_{12} = H^{24}b_{23} - H^{25}\left(b_{22} - \lambda_j^2\right)$. These asymptotic solutions can be interpreted as normalized by the first component of each vector. With the same normalization, the asymptotic solutions are at the same scale.

References

[1] X. Zhong, X. Wang, Direct numerical simulation on the receptivity, instability, and transition of hypersonic boundary layers, Annu. Rev. Fluid Mech. 44 (2012) 527–561.

[2] M.V. Morkovin, Transition in open flow systems-a reassessment, Bull. Am. Phys. Soc. 39 (1994) 1882.

[3] W.S. Saric, H.L. Reed, E.J. Kerschen, Boundary-layer receptivity to freestream disturbances, Annu. Rev. Fluid Mech. 34 (2002) 291–319.

[4] S. He, X. Zhong, Hypersonic boundary-layer receptivity over a blunt cone to freestream pulse disturbances, AIAA J. 59 (2021) 3546–3565.

[5] Y. Ma, X. Zhong, Receptivity of a supersonic boundary layer over a flat plate. Part 1. Wave structures and interactions, J. Fluid Mech. 488 (2003) 31–78.

[6] H. Salwen, C.E. Grosch, The continuous spectrum of the Orr-Sommerfeld equation. Part 2. Eigenfunction expansions, J. Fluid Mech. 104 (1981) 445–465.

[7] A. Tumin, A. Fedorov, Spatial growth of disturbances in a compressible boundary layer, J. Appl. Mech. Tech. Phys. 24 (1983) 548–554.

[8] L.M. Mack, Boundary-layer linear stability theory, Technical Report, California Inst of Tech Pasadena Jet Propulsion Lab, 1984.

[9] A. Fedorov, A. Tumin, High-speed boundary-layer instability: old terminology and a new framework, AIAA J. 49 (2011) 1647–1657.

[10] A. Fedorov, Transition and stability of high-speed boundary layers, Annu. Rev. Fluid Mech. 43 (2011) 79–95.

[11] L.M. Mack, A numerical study of the temporal eigenvalue spectrum of the Blasius boundary layer, J. Fluid Mech. 73 (1976) 497–520.

[12] C.E. Grosch, H. Salwen, The continuous spectrum of the Orr-Sommerfeld equation. Part 1. The spectrum and the eigenfunctions, J. Fluid Mech. 87 (1978) 33–54.

[13] V. Zhigulev, N. Sidorenko, A. Tumin, The generation of instability waves in a boundary layer having external turbulence, PMTF Zh. Prikl. Mekh. Tekhn. Fiz. (1980) 43–49.

[14] M.R. Scott, H.A. Watts, Computational solution of linear two-point boundary value problems via orthonormalization, SIAM J. Numer. Anal. 14 (1977) 40–70.

[15] A. Tumin, Multimode decomposition of spatially growing perturbations in a two-dimensional boundary layer, Phys. Fluids 15 (2003) 2525–2540.

[16] A. Tumin, Three-dimensional spatial normal modes in compressible boundary layers, J. Fluid Mech. 586 (2007) 295–322.

[17] M. Malik, Numerical methods for hypersonic boundary layer stability, J. Comput. Phys. 86 (1990) 376–413.

[18] C.L. Haley, X. Zhong, Mode F/S Wave Packet Interference and Acoustic-Like Emissions in a Mach 8 Flow over a Cone, AIAA, 2020, https://arc.aiaa.org/doi/abs/10.2514/6.2020-1579.

[19] S. He, X. Zhong, The effects of nose bluntness on broadband disturbance receptivity in hypersonic flow, Phys. Fluids 34 (2022) 054104.

[20] A. Varma, X. Zhong, Hypersonic Boundary-Layer Receptivity to a Freestream Entropy Pulse with Real-Gas and Nose Bluntness Effects, AIAA, 2020, https://arc.aiaa.org/doi/abs/10.2514/6.2020-2994.

[21] X. Zhong, High-order finite-difference schemes for numerical simulation of hypersonic boundary-layer transition, J. Comput. Phys. 144 (1998) 662–709.

[22] X. Zhong, M. Tatineni, High-order non-uniform grid schemes for numerical simulation of hypersonic boundary-layer stability and transition, J. Comput. Phys. 190 (2003) 419–458.

[23] R.K. Shukla, M. Tatineni, X. Zhong, Very high-order compact finite difference schemes on non-uniform grids for incompressible Navier–Stokes equations, J. Comput. Phys. 224 (2007) 1064–1094.

[24] C.H. Mortensen, X. Zhong, Real-gas and surface-ablation effects on hypersonic boundary-layer instability over a blunt cone, AIAA J. 54 (2016) 980–998.

[25] P. Gaydos, A. Tumin, Multimode decomposition in compressible boundary layers, AIAA J. 42 (2004) 1115–1121.

[26] L.M. Mack, Transition and laminar instability, Technical Report, 1977.

[27] E.C. Marineau, Prediction methodology for second-mode-dominated boundary-layer transition in wind tunnels, AIAA J. 55 (2017) 484–499.

[28] Y. Huang, X. Zhong, Numerical study of hypersonic boundary-layer receptivity with freestream hotspot perturbations, AIAA J. 52 (2014) 2652–2672.

[29] A. Tumin, The biorthogonal eigenfunction system of linear stability equations: a survey of applications to receptivity problems and to analysis of experimental and computational results, in: 41st AIAA Fluid Dynamics Conference and Exhibit, 2011, p. 3244.

[30] B. Saikia, S. Al Hasnine, C. Brehm, On the role of discrete and continuous modes in a cooled high-speed boundary layer flow, J. Fluid Mech. 942 (2022) R7.

[31] S.M.A.A. Hasnine, V. Russo, O.M. Browne, A. Tumin, C. Brehm, Disturbance Flow Field Analysis of Particulate Interaction with High Speed Boundary Layers, AIAA, 2020, https://arc.aiaa.org/doi/abs/10.2514/6.2020-3046.

[32] S.A. Al Hasnine, V. Russo, A. Tumin, C. Brehm, Biorthogonal decomposition of the disturbance flow field generated by particle impingement on a hypersonic boundary layer, J. Fluid Mech. 969 (2023) A1.

[33] A. Tumin, X. Wang, X. Zhong, Numerical simulation and theoretical analysis of perturbations in hypersonic boundary layers, AIAA J. 49 (2011) 463–471.

[34] M. Miselis, Y. Huang, X. Zhong, Modal Analysis of Receptivity Mechanisms for a Freestream Hot-Spot Perturbation on a Blunt Compression-Cone Boundary Layer, AIAA, 2016, https://arc.aiaa.org/doi/abs/10.2514/6.2016-3345.

[35] B.J. McKeon, A.S. Sharma, A critical-layer framework for turbulent pipe flow, J. Fluid Mech. 658 (2010) 336–382.

[36] M.R. Jovanović, B. Bamieh, Componentwise energy amplification in channel flows, J. Fluid Mech. 534 (2005) 145–183.

[37] A. Dwivedi, G.S. Sidharth, M.R. Jovanović, Oblique transition in hypersonic double-wedge flow, 2021, https://arxiv.org/abs/2111.15153.

[38] D.A. Cook, J. Thome, J.M. Brock, J.W. Nichols, G.V. Candler, Understanding effects of nose-cone bluntness on hypersonic boundary layer transition using input-output analysis, AIAA, 2018, https://arc.aiaa.org/doi/abs/10.2514/6.2018-0378.

[39] J.W. Nichols, G.V. Candler, Input-output analysis of complex hypersonic boundary layers, AIAA, 2019, https://arc.aiaa.org/doi/abs/10.2514/6.2019-1383.

[40] J. Bae, S.T. Dawson, B.J. McKeon, Studying the effect of wall cooling in supersonic boundary layer flow using resolvent analysis, AIAA, 2020, https://arc.aiaa.org/doi/abs/10.2514/6.2020-0575.

[41] B.T. Chu, On the energy transfer to small disturbances in fluid flow (part I), Acta Mech. 1 (1965) 215–234.

[42] Z. Zou, X. Zhong, A High-Order Finite-Difference Method for Linear Stability Analysis and Bi-Orthogonal Decomposition of Hypersonic Boundary Layer Flow, 2023, https://arc.aiaa.org/doi/abs/10.2514/6.2023-1043.

[43] D. Kosloff, H. Tal-Ezer, A modified Chebyshev pseudospectral method with an o(n-1) time step restriction, J. Comput. Phys. 104 (1993) 457–469.

[44] P. Balakumar, M.R. Malik, Discrete modes and continuous spectra in supersonic boundary layers, J. Fluid Mech. 239 (1992) 631–656.

[45] A. Fedorov, A. Khokhlov, Prehistory of instability in a hypersonic boundary layer, Theor. Comput. Fluid Dyn. 14 (2001) 359–375.